Title
Dlx1 and the NuRD Complex Cooperate to Regulate Enhancer Activity in the Developing Subpallium

Author
Price, James D'Aloia

Publication Date
2020

Peer reviewed|Thesis/dissertation

Dlx1 and the NuRD Complex Cooperate to Regulate Enhancer Activity in the Developing Subpallium

by

James D'Aloia Price

DISSERTATION

Submitted in partial satisfaction of the requirements for degree of

DOCTOR OF PHILOSOPHY

in

Developmental and Stem Cell Biology

in the

GRADUATE DIVISION

of the

UNIVERSITY OF CALIFORNIA, SAN FRANCISCO

Approved:

DocuSigned by:

Brian Black

BE1B184BD52347A...

Brian Black

Chair

DocuSigned by:

Benoit G. Bruneau

DocuSigned by:

John Rubenstein

44A19A16E413450...

Committee Members

Acknowledgements

I would like to express my gratitude to my PhD advisor and mentor Dr. John Rubenstein for his support and guidance throughout the duration of my training in the lab. His deep base of knowledge, adaptability, and keen eye for detail were instrumental in driving this project to completion. John's patience and compassion helped to support me in working through difficult and seemingly intractable problems, and the skills I have learned in his lab have helped me to become a more capable and resilient person.

I am also indebted to my thesis committee members Dr. Brian Black and Dr. Benoit Bruneau. Both Benoit and Brian provided invaluable feedback which helped me to broaden my thinking, provided new perspectives on data, and provided critical support to help my project reach fruition.

Also instrumental in my success throughout my degree were my amazing colleagues in the lab. Susan Lindtner, who provided mentorship from my very earliest stages in lab through to today, always looked out for not only the wellbeing of my project, but also my own wellbeing. She is an amazing scientist, friend, and role model who helped to support me even in the toughest of times. Athena Ypsilanti, whose passion for new and exciting science helped to stoke the fires of my own creativity. She managed to help me push the boundaries of what I saw as possible, all the while maintaining an amazing sense of humor which never failed to keep the lab in high spirits. Eirene Markenscoff-Papadimitriou, who always helped to provide insightful feedback and encouragement. And to Anna Rubin and Magnus Sandberg, who helped me to overcome obstacles and setbacks through their many late-night consultations of my project. I am also extremely proud and grateful to have been given the opportunity to mentor three amazing students during my time in the lab: Lorraine Abellan, Queenie Lin, and Fadya Binyameen. My thanks to them for bringing fresh eyes and enthusiasm to the lab, as seeing them succeed and go on to their own postgraduate studies has brought me happiness.

A huge thank you to Carol Kim, whose selfless stewardship of the lab helped push my project farther and faster than would be otherwise possible. Thank you to Jeff Johnson, Gwen Jang, and Billy Newton for their assistance with immunoprecipitation and mass spectroscopy. Thank you to Dr. Alex Nord and Rinaldo Catta-Preta for their support with bioinformatic analysis. Thank you to Diane Dickel, Jennifer Akiyama, and the rest of the team with the VISTA Enhancer Browser for their assistance with obtaining transient transgenic enhancer embryos.

Finally, to my mother Jewel. The completion of this work was only possible with her unconditional love and unwavering support. She is an incredible role model and mentor, and without her I could not have come this far.

Dedicated to the memory of **Rita D'Aloia**

Dlx1 and the NuRD Complex Cooperate to Regulate Enhancer Activity in the Developing Subpallium

by James D'Aloia Price

Abstract

The embryonic subpallium generates neurons and glia which contribute to the functional diversity of the brain. Proper spatial and temporal generation of these cells relies on complex molecular mechanisms which control transcription through regulation of genome architecture. As the progeny of stem cells of the subpallium differentiate, the fate decision between neurons and glia is driven by expression of *Dlx1/2* or *Olig1/2* respectively, two sets of transcription factors (TFs) with a mutually repressive relationship. The mechanism by which TFs such as *Dlx1/2* can repress alternative cell fates while simultaneously promoting transcription of genes required for differentiation, however, is not yet fully understood. Using immunoprecipitation *in vitro* and *in vivo*, we found that DLX1 interacts with the nucleosome remodeling complex NuRD through an interaction with RBBP4 and RBBP7. We observed that a reduction in the levels of RBBP4/7 in the developing telencephalon leads to a variety of developmental defects, including a reduction in cell division and interneuron production. ChIP-seq studies of genomic occupancy of DLX1 and six different members of the NuRD complex show that DLX1 and NuRD colocalize to putative regulatory elements (pREs) enriched near other transcription factors, and that loss of *Dlx1/2* leads to dysregulation of genome accessibility at pREs near genes repressed by *Dlx1/2*. We identified an *Olig2* pRE which has activity in the forebrain, remains accessible in *Dlx1/2* mutants, and is bound by DLX1 and the NuRD complex. Consequently, heterozygosity of *Dlx1/2* and *Rbbp4* leads to an increase in the production of OLIG2+ cells. Together these findings suggest a mechanism by which *Dlx1* cooperates with the NuRD complex to regulate transcription of target genes by altering the chromatin state of regulatory elements. These

findings underscore the critical role of the NuRD complex during development and point to the interaction between TFs and chromatin remodelers as a mechanism underlying cell fate decisions.

Table of Contents

List of Figures

List of Tables

Chapter 1

Introduction and Background

Throughout development, cell fate is progressively restricted as cells differentiate from multipotent self-renewing progenitors to differentiated cells. These differentiation events are tightly controlled through progressive rounds of symmetric and asymmetric cell divisions of progenitors in both a spatial and temporal fashion, and failures in the timing or frequency of cell differentiation events in the embryonic brain lead to developmental disorders.

Differentiation events are accompanied by changes in transcriptional patterns and genome architecture, as cells promote genes which drive differentiation and maturation in favor of self-renewal programs. These changes in gene expression are mediated by the combinatorial expression of Transcription Factors (TFs). TFs bind to specific DNA motifs at regulatory elements (REs) and control transcription of target genes, including other TFs, leading to a cascade of transcriptional changes as cells differentiate (Dubois-Chevalier et al., 2018; Nord et al., 2015).

The mechanisms by which cell-type specific transcription factors can simultaneously activate and repress gene expression in a context-dependent manner are still not fully understood. This aim of this study is to in part answer this question by interrogating the interaction between a cell-type specific TF and a chromatin remodeling complex and assessing the consequences of disrupting this interaction on cell fate.

1A. Subpallial development and the role of DLX transcription factors

The embryonic basal ganglia (BG) are subpallial structures composed of three ganglionic eminences (GE), the medial ganglionic eminence (MGE), the lateral ganglionic eminence (LGE), and caudal ganglionic eminence (CGE). The GEs give rise to GABAergic projection neurons of the striatum, globus pallidus, and amygdala, as well as interneurons which migrate throughout the cortex and hippocampus (Silberberg et al., 2016, Lim et al., 2018). The embryonic BG is composed of three layers: the ventricular zone (VZ) where tripotent neural stem cells called radial glia reside and give rise to intermediate progenitors which populate the subventricular zone (SVZ),

and the mantle zone (MZ) where postmitotic cells either settle or migrate to their final site of integration (Garcia and Harwell, 2017).

The generation and differentiation of GABAergic neurons depend on a transcriptional network controlled by the DLX homeodomain TFs encoded by *Dlx1, Dlx2, Dlx5* and *Dlx6* (Anderson et al., 1997; Eisenstat et al. 1999; Long et al. 2009, Lindtner et al. 2019). *Dlx* genes are expressed in a temporal sequence as cells differentiate: *Dlx2*, *Dlx1*, *Dlx5* and finally *Dlx6* (Eisenstat et al., 1999; Zerucha et al., 2000; Panganiban and Rubenstein, 2002). *Dlx2* is first expressed in the telencephalon in neuroepithelial cells at E10, followed shortly by *Dlx1*. The *Dlx* TFs continue to be expressed throughout subpallial development and are maintained into adulthood in a subset of GABAergic cortical interneurons (Pla et al., 2018). Deletion of *Dlx1* and *Dlx2* in mouse leads to a block in the differentiation of forebrain GABAergic neuronal progenitors caused by deregulation of gene patterning and expression. *Dlx1* and *Dlx2* repress the transcription of genes that promote the progenitor state and glial fate, whereas they activate transcription of genes that promote GABAergic neuronal differentiation (Long et al. 2009, Lindtner et al. 2019). For instance, *Dlx* TFs have a mutually repressive relationship with *Olig1* and *Olig2*, bHLH TFs which promote differentiation of oligodendrocytes (Petryniak et al. 2007; Silbereis et al. 2014). *Dlx* TFs are expressed at high levels in SVZ and MZ cells, but only in a few sparse cells in the VZ, in keeping with the evidence that DLX proteins promote BG neuronal differentiation (Long et al. 2009). The balance between neurogenesis and oligodendrogenesis is thus mediated by these two sets of opposing transcriptional regulators.

1B. Epigenetic regulation of transcription in the subpallium

In eukaryotes, transcription is regulated through the interaction of promoters and regulatory elements (REs) such as enhancers (Levine et al., 2014). The activity of both promoters and REs is regulated at the chromatin level in processes that control the temporal and spatial regulation of gene expression during development (Hsieh and Gage, 2005; Long et al. 2016; Hirabayashi and

Gotoh, 2010; Nord et al., 2015). While combinatorial expression of TFs is known to drive the complex processes of neuronal differentiation and maturation, it is becoming clear that proteins which alter chromatin state also play a critical role during embryonic neural development, as disruption of chromatin remodeling genes has been implicated in developmental delay, intellectual disability, autism, and schizophrenia (Satterstrom et al. 2020; Sanders et al. 2015; De Rubeis et al. 2014).

There are several mechanisms by which chromatin modifying enzymes regulate gene expression, including DNA methylation, covalent modifications of Histone tails, and ATP-dependent nucleosome remodeling (Moore et al. 2013; Bannister, and Kouzarides, 2011; Narlikar et al. 2013). REs can be identified by a uniue epigenetic signature: a central region with a low density of nucleosomes and high accessibility flanked by nucleosomes with high levels of H3K4me1 and low levels of H3K4me3 (Bonn et al., 2012; Creyghton et al. 2010). Additionally, acetylation of H3K27 by Histone acetyltransferase p300 is associated with active enhancer and promoter states, while methylation by the polycomb repressive complex PRC2 is associated with a poised or repressed state (Blanco et al. 2020; Creyghton et al. 2010; Rada-Iglesias et al. 2015). Histone deacetylase enzymes (HDAC) facilitate the removal of the acetyl mark from Histones and thus facilitating the deposition of H3K27me3 in some cases (Cao et al. 2002; Kim et al. 2015). The NuRD complex is unique among epigenetic regulators, as it is one of the few known to couple histone deacetylase and nucleosome remodeling activity within the same complex (Zhang et al., 1998; Tyler and Kadonaga, 1999).

1C. Structure and Function of the NuRD complex

The exact composition of the NuRD complex is variable, as epigenetic complexes such as NuRD often contain interchangeable subunits. Some of these subunits are mutually exclusive or expressed at different levels in different cell types, altering the function and substrate specificity of the complex (Nitarska et al., 2016; Le Guezennec et al., 2006; Schmidberger et al., 2016).

Nearly every member of the canonical complex contains at least one paralogue which can take its place in the complex; these are RBBP4/7, HDAC1/2, MTA1/2, GATAD2A/B, MBD2/3, CHD3/4/5 (Zhang et al., 1999; Smits et al., 2013). A sub-complex of NuRD consisting of RBBP4/7, MTA1/2, and HDAC1/2 also associates with the proteins PWWP2A/B and promotes gene expression by regulating levels of Histone H4K36 acetylation (Link et al., 2018; Zhang et al., 2018). NuRD subunits such as MBD2/3 can bind methylated DNA directly, however interactions of NuRD with TFs allow it to be targeted to specific genomic loci (Spruijt et al., 2016; Wu et al., 2016; Basta et al., 2017; Hong et al., 2005, Moody et al., 2018).

Towards identifying biochemical mechanisms through which DLX1/2 control gene expression in the BG, Lindtner et al. (2019) demonstrated that the DLX1, 2 and 5 bind to promoter, intergenic and intronic REs where they either activate or repress the activity of nearby genes. Loss of *Dlx1/2* leads to changes in Histone H3 posttranslational modifications that correlate with changes in RNA levels, indicating that DLX TFs participate in epigenetic regulation of these loci, however the biochemical mechanism for this is unknown. In this study, we describe the role of NuRD components *Rbbp4* and *Rbbp7* in BG progenitors and present evidence that their interaction with DLX1 promotes transcriptional repression by modifying the chromatin state of REs.

Chapter 2

Identification of an interaction between DLX1 and RBBP4

2A. Screen for DLX1 interacting proteins

To discover proteins that interact with DLX TFs, we generated a mouse *Dlx1* knock-in allele that fuses a 3XFLAG tag (FLAG) to the C-terminus of DLX1 followed by an IRES GFP reporter **(Fig. 2.1A**). GFP expression in the forebrain at embryonic day 13.5 (E13.5) matched RNA expression of *Dlx1* (**Fig. 2.1A**). Because DLX1 is localized to the nucleus (**Fig. 2.1B**), we performed cellular fractionation to remove cytoplasmic proteins and treated nuclear lysates with Benzonase to minimize protein-protein interactions mediated through DNA or RNA. We then performed immunoprecipitation (IP) with anti-FLAG monoclonal antibody and eluted proteins using a 100X molar excess of FLAG peptide. We performed three independent IPs from nuclear extracts derived from BG of E13.5 $Dlx1^{FLAG}$ or WT embryos and identified eluted proteins using tandem mass spectroscopy. We identified peptides which mapped to DLX1 in IP eluates from $Dlx1^{FLAG}$ animals, however their abundance was low (<1% of all mapped peptides) and no other protein met a statistically significant threshold for enrichment. Nonetheless, multiple peptides corresponding to proteins of the NuRD and BAF complexes were present at higher levels in $Dlx1^{FLAG}$ IP than WT samples (**Table 2.1**). This result supports previous work showing two members of the BAF complex, BRG1 (SMARCA4) and BAF170 (SMARCC2), associate with DLX1 based on the findings of mass spectroscopy using a pan-DLX antibody (Cajigas et al., 2015). One protein identified, RBBP4, associates with both the NuRD complex and polycomb complex PRC2 (Kuzmichev et al., 2002), however we did not observe any members of the PRC2 complex in our mass spectroscopy experiments.

To validate the mass spectroscopy results, we co-expressed DLX1-FLAG with StrepII-tagged subunits from the NuRD complex in HEK293T cells and assayed for interactions with DLX1 using IP followed by Western Blot. Of all the NuRD subunits tested, RBBP4 demonstrated the most robust interaction with DLX1 (**Fig. 2.2A,** data not shown). Supporting these results, we

found that the RBBP4-DLX1 interactions were reproducible in NaCl concentrations up to 500mM and in the presence of Benzonase, DNase, and RNase (**Fig. 2.2B**, **2.2C**).

Because these experiments rely on the use of tagged proteins which are expressed above their physiological levels, we sought to determine whether the DLX1-RBBP4 interaction was reproducible *in vivo*. Both immunostaining and *in situ* hybridization (ISH) show that DLX1 and RBBP4 overlap in cells of the ventricular zone (VZ) and subventricular zone 1 (SVZ1) (**Fig. 2.3A-C**). Using nuclear extracts, we observed that DLX1 interacts with both RBBP4 and its paralog RBBP7 *in vivo* (**Fig. 2.3D**). To test whether DLX1 was able to interact with either the NuRD or PRC2 complex, we performed a DLX1 IP, followed by CHD4 and EZH2 immunoblotting. We found that antibodies to RBBP4, RBBP7, and DLX1 were all able to IP CHD4, while only RBBP4 was able to strongly IP EZH2 (**Fig. 2.3D**). Thus, we conclude that DLX1 interacts with NuRD, but not PRC2, likely through its interaction with RBBP4 and RBBP7.

2B. Identification of a RBBP4 binding domain within DLX1

Previous studies have found that RBBP4 interacts with the BCL11A/B, SALL1/4, and ZFPM1 (FOG1) TFs through a canonical MSRRKQ motif found at the N-terminus of each protein (Moody et al., 2018, Basta et al., 2017; Hong et al., 2005). RBBP4 also interacts with PHF6 and PRDM16 through regions containing a high density of Lysine and Arginine residues, but which lack significant homology to the MSRRKQ motif (**Fig. 2.4A**) (Liu et al., 2015, Ivanochko et al., 2019, Sankaran et al., 2008). To identify a region in DLX1 that mediates an interaction with RBBP4, we co-transfected truncated forms of DLX1 with RBBP4 in HEK 293T cells and compared the interactions using IP and immunoblotting (**Fig. 2.4B-D**). The N-terminus (amino acids 1-129) was found to interact weakly with RBBP4, however deletion of the N-terminus led to a large reduction in binding compared to C-terminal deletion, suggesting that the interaction motif may be located at the boundary of the N-terminus and homeodomain (**Fig. 2.4B, 2.4C**). This boundary region contains a sequence with a high density of lysine and arginine residues (124-132,

KGKKIRKPR) characteristic of other bona-fide RBBP4 interaction motifs (**Fig. 2.4A**). A deletion immediately upstream of KKIRKPR (Δ120-125, Fig. 2D) had a minimal impact on DLX1 binding to RBBP4, whereas substitution of this domain with Alanine (mut1, **Fig. 2.4E, 2.4F**) greatly reduced both RBBP4 and RBBP7 binding to DLX1. Replacement of four of the six positively charged amino acids in this region (mut 5, **Fig. 2.4E, 2.4F**) similarly diminished the ability of DLX1 to bind to RBBP4 and RBBP7, suggesting that these Arginine and Lysine residues are critical for the interaction between DLX1 and RBBP4/7.

Table 2.1: Proteins of the NuRD and BAF complexes Identified by IP/Mass Spectroscopy

Protein Name	Dlx1FLAG rep1	Dlx1FLAG rep2	Dlx1FLAG rep3	Dlx1FLAG total	Control rep1	Control rep2	Control rep3	Control total
DLX1	10	14	17	**41**	0	3	0	**3**
BCL11A	0	1	3	**4**	0	0	0	**0**
BCL11B	1	3	3	**7**	0	0	0	**0**
CDK2AP1	0	0	2	**2**	0	0	1	**1**
CHD4	0	0	13	**13**	0	0	2	**2**
CHD5	0	1	9	**10**	0	1	4	**5**
GATAD2A	0	2	2	**4**	0	0	2	**2**
GATAD2B	0	4	12	**16**	0	3	4	**7**
HDAC1	3	1	13	**17**	0	1	3	**4**
HDAC2	0	0	17	**17**	0	0	2	**2**
KDM1A	0	0	9	**9**	0	0	2	**2**
MBD3	0	5	7	**12**	0	4	5	**9**
MTA1	0	0	12	**12**	0	0	9	**9**
MTA2	2	2	13	**17**	0	1	5	**6**
MTA3	0	0	0	**0**	0	0	0	**0**
RBBP4	3	8	22	**33**	1	10	5	**15**
RBBP7	1	2	12	**15**	0	1	3	**4**
ACTL6A	0	2	12	**14**	0	1	2	**3**
ACTL6B	0	0	1	**1**	0	0	1	**1**
ARID1A	0	4	18	**22**	0	4	7	**11**
DPF1	0	0	4	**4**	0	0	0	**0**
DPF2	0	1	6	**7**	0	0	3	**3**
SAP18	0	0	0	**0**	0	0	0	**0**
SMARCA4	0	2	19	**21**	0	2	10	**12**
SMARCA5	3	0	3	**6**	0	0	1	**1**
SMARCB1	0	1	10	**11**	0	0	5	**5**
SMARCC1	0	2	8	**10**	0	0	5	**5**
SMARCC2	0	9	18	**27**	0	5	10	**15**
SMARCD1	0	0	3	**3**	0	0	1	**1**
SMARCD3	0	1	5	**6**	0	0	3	**3**
SMARCE1	0	4	10	**14**	0	2	10	**12**
SS18	0	0	1	**1**	0	0	0	**0**
SS18L1	0	2	3	**5**	0	1	1	**2**

Selected results from three biological replicates each from anti-3XFLAG immunoprecipitation (IP) from BG of *Dlx1*^{FLAG} (Dlx1FLAG) or WT (Control) E13.5 embryos. Numbers for each replicate represent the number of unambiguously mapped peptides for each protein. DLX1 is highlighted in yellow, NuRD subunits are highlighted in blue, and BAF subunits are highlighted in green.

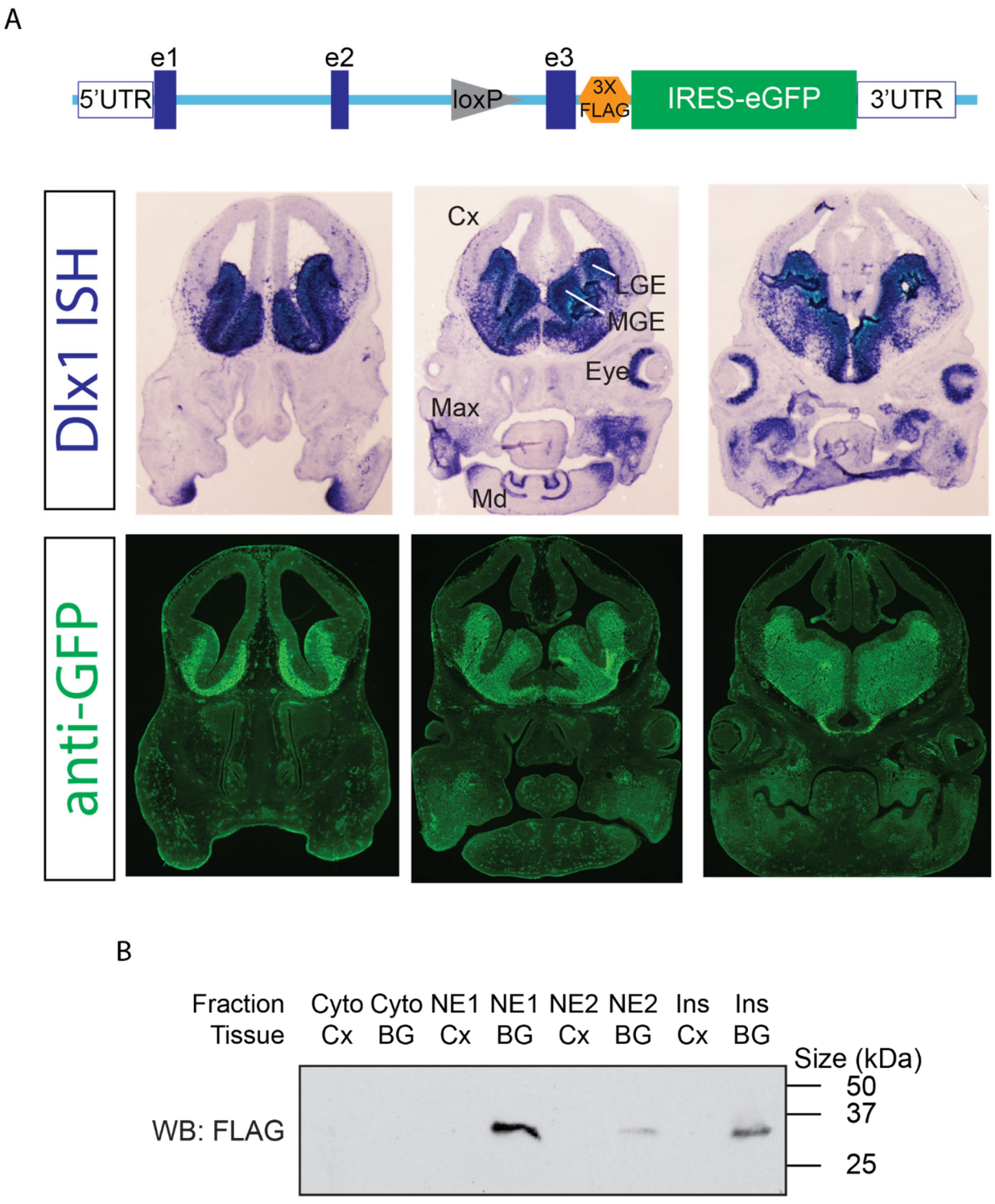

Figure 2.1: Purification of DLX1 protein from Dlx1^{FLAG} transgenic mice

A. Schematic of the knock-in Dlx1^{FLAG} transgene which expresses DLX1 with a C-terminal 3XFLAG tag followed by IRES and eGFP. Middle panels show normal pattern of *Dlx1* RNA as assessed by *in situ* hybridization in E13.5 *Dlx1*$^{FLAG/FLAG}$ embryos. Bottom panels show native expression of GFP from transgenic animals. Images are arranged from rostral (left) to caudal

(right). Cx: cortex; Max: Maxilla; Md: mandible; LGE; lateral ganglionic eminence, MGE; medial ganglionic eminence. **B.** Western blot of DLX1-FLAG following cell fractionation procedure from E13.5 BG and cortex (Cx) of *Dlx1*$^{FLAG/+}$ transgenic mice. DLX1 protein is present in BG nuclear extracts. Cyto: Cytoplasm, NE1: nuclear extract following first addition of extraction buffer, NE2: nuclear extract following a subsequent addition of extraction buffer, Ins: insoluble fraction.

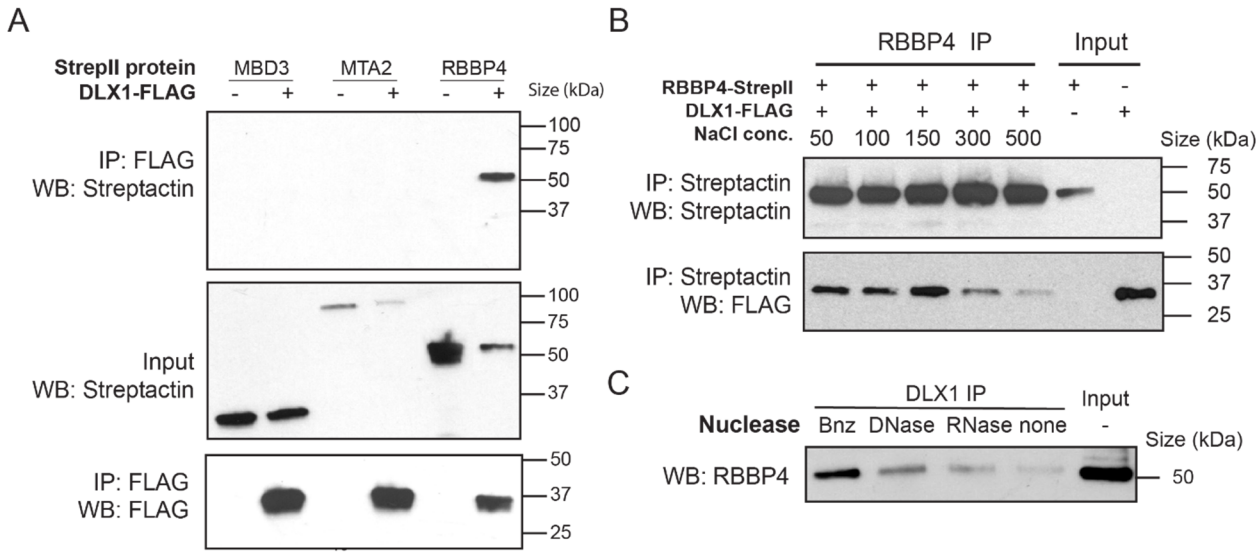

Figure 2.2: DLX1 binds RBBP4 *in vitro*

A. Western blots of immunoprecipitations from HEK 293T cells cotransfected with FLAG-tagged DLX1 and StrepII-tagged NuRD complex proteins (MBD3, MTA2 and RBBP4). Top Panel: Immunoprecipitation (IP) with anti-FLAG antibody followed by Western blot (WB) with Streptactin, showing that only RBBP4 co-IPs with DLX1. Middle Panel: shows that the StrepII-tagged NuRD complex proteins were expressed and had the expected molecular weights. Bottom panel: IP (immunoprecipitation) of DLX1-FLAG with anti-FLAG antibody followed by WB (western blot) with anti-FLAG antibody, showing efficiency of FLAG immunoprecipitation.**B.** WB showing IP of RBBP4 (StrepII tagged) and DLX1 (FLAG tagged) in the presence of up to 500mM NaCl. Proteins were expressed separately in HEK 293T cells and whole cell lysates containing each were mixed along with NaCl at concentrations indicated prior to IP. Top panel: control WB with Streptactin. Bottom panel: WB with anti-FLAG showing sensitivity of RBBP4-DLX1 interaction to NaCl concentration. **C.** DLX1-FLAG IP from E13.5 BG of *Dlx1*$^{FLAG/+}$ transgenic mice followed by WB with anti-RBBP4. IPs were performed in the presence of three nucleases. From left to right: Bnz, Benzonase (DNase and RNase); DNase, deoxyribonuclease I; RNase, ribonuclease A. Benzonase was the most efficient in enabling the detection of RBBP4 following the DLX1 IP; this also provides evidence that the DLX1-RBBP4 interaction does not depend on DNA or RNA.

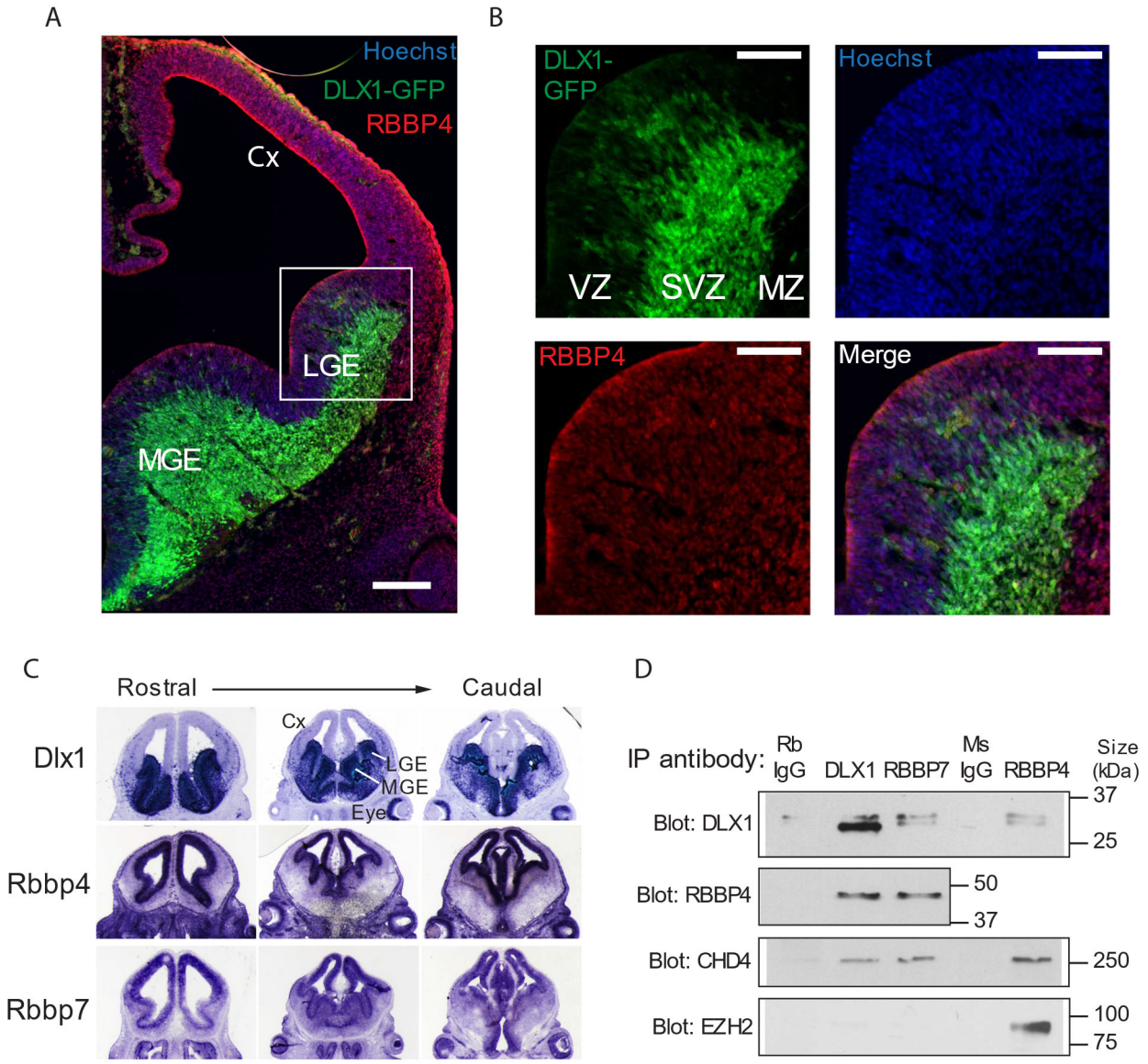

Figure 2.3: RBBP4 and DLX1 have overlapping expression and bind *in vivo*

A. Immunostaining of RBBP4 (red) in E13.5 coronal sections of *Dlx1*$^{FLAG/+}$ embryos. DLX1-GFP is native fluorescence from GFP-expressing transgene. Cx; Cortex; LGE: lateral ganglionic eminence, MGE: medial ganglionic eminence. Scale bar: 200μm.**B.** High magnification images of inset from panel D showing scattered GFP cells in VZ and strong GFP expression in SVZ and MZ. VZ: ventricular zone, SVZ: subventricular zone, MZ: mantle zone. Scale bar: 100μm.**C.** *In situ* hybridization using probes to *Dlx1*, *Rbbp4*, and *Rbbp7* showing RNA expression in the LGE, MGE and Cx in E13.5 coronal sections.**D.** Immunoprecipitation of native DLX1, RBBP4, and RBBP7 from nuclear extracts of E13.5 *Dlx1*$^{FLAG/+}$ basal ganglia (BG) tissue, followed by WB using anti-DLX1, anti-RBBP4, anti-CHD4 and anti-EZH2, showing evidence for reciprocal interactions between DLX1, RBBP4 and CHD4. White arrowhead indicates untagged DLX1 protein, black arrowhead indicates DLX1-FLAG protein produced by *Dlx1*^{FLAG} locus.

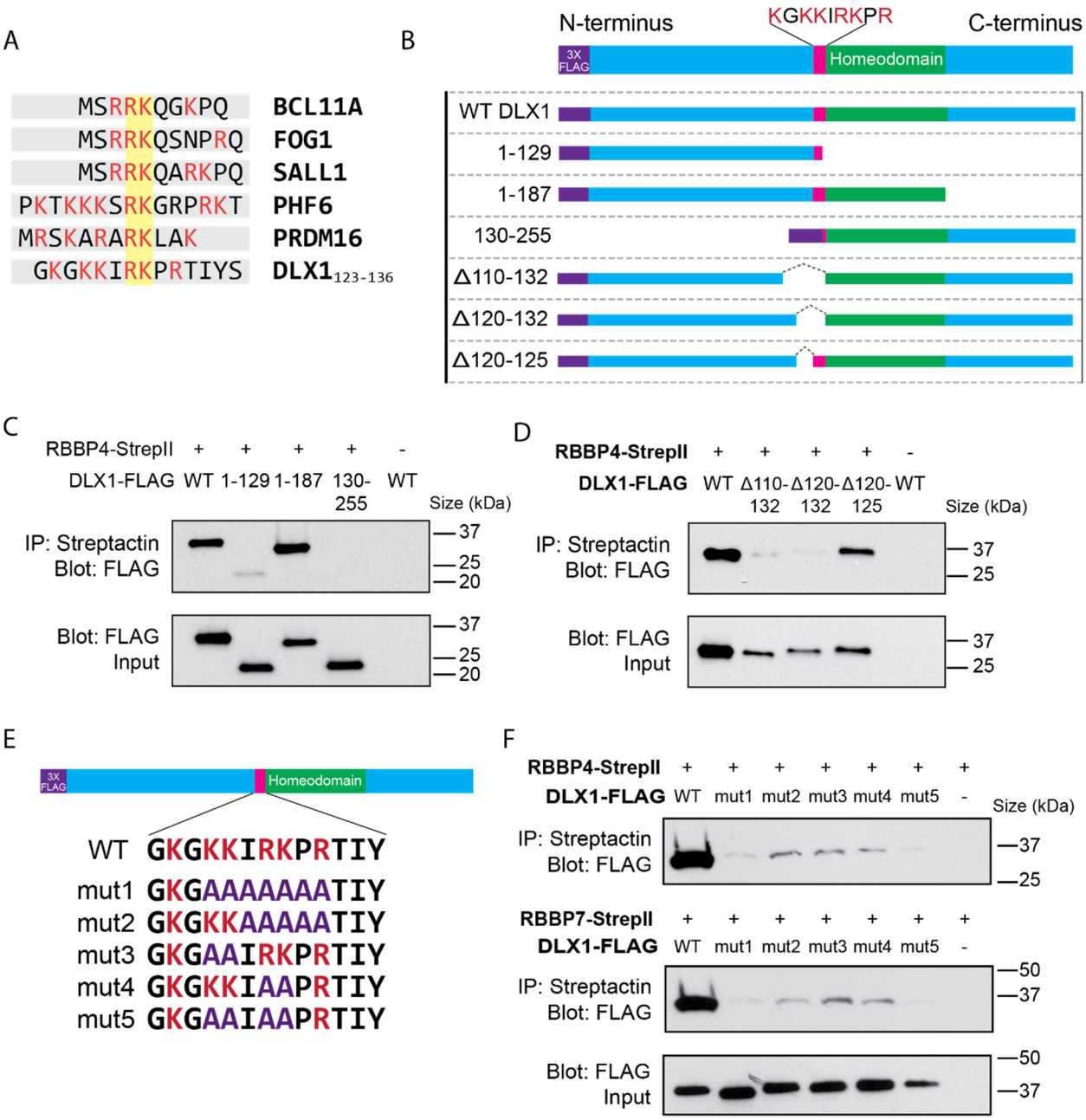

Figure 2.4: Identification of a RBBP4 binding motif in DLX1

A. Comparison of interaction motifs of five transcription factors known to bind RBBP4 and candidate interaction domain within DLX1 (amino acids 123-136). Arginine and Lysine residues are in red; a common RK peptide is highlighted in yellow. **B.** Schematic of domains of N-terminally tagged DLX1-FLAG protein. Shown are WT DLX1, two C-terminal deletions, one N-terminal deletion, and three internal deletions (D) of the candidate RBBP4 interaction domain. Amino acid numbers are indicated on the left. **C,D.** HEK 293T cells were cotransfected with RBBP4-StrepII and with either the full-length DLX1-FLAG or its various truncations and internal deletions shown in panel B. RBBP4-StrepII was precipitated using Streptactin magnetic beads. Top Panel: IP with Streptactin antibody followed by WB with FLAG showing which DLX1 truncation mutants were able to coimmunoprecipiate (coIP) with RBBP4-StrepII. Bottom Panel: shows that DLX1

truncation mutants were expressed at similar levels in the various transfections and at the expected molecular weights. **E.** Schematic of DLX1 protein (top) with the amino acid sequences of the putative RBBP4/7 interaction motif and five Alanine substitution mutants of amino acids 126-132 shown below. Lysine and Arginine residues are red and amino acids replaced by Alanine are purple. **F.** HEK 293T cells were cotransfected with RBBP4-StrepII or RBBP7-StrepII and either full-length FLAG-tagged DLX1 or the various alanine substitutions shown in panel E. RBBP4-StrepII (top panel) or RBBP7-StrepII (middle panel) was precipitated using Streptactin magnetic beads and studied using WBs labeled with anti-FLAG antibody. Bottom Panel: shows that DLX1 proteins were expressed at similar levels in the various transfections and at the expected molecular weights.

Chapter 3

Consequences of *Rbbp4/Rbbp7* loss of function mutations

3A. Phenotypes of *Rbbp4* and *Rbbp7* single mutants

The NuRD complex plays a critical role throughout development and into adulthood as an epigenetic regulator. Loss of function of NuRD subunits can lead to a variety of phenotypes including embryonic lethality, cell specification defects, or altered synaptic plasticity (Spengler and Hoffmann, 2019; Pavlopoulos et al., 2013). Despite the importance of NuRD across a variety of cell types, the functions of *Rbbp4* and *Rbbp7* during post-implantation development are unknown. ISH shows that expression of *Rbbp4, Rbbp7* and other NuRD members, except *Chd5,* are expressed most highly in progenitors of the telencephalon (VZ and SVZ) at E13.5, with lower expression in differentiating neurons of the mantle zone (MZ) (**Fig. 3.1)**.

To understand the consequences of loss of function of *Rbbp4* and *Rbbp7*, we obtained a constitutive null allele of *Rbbp4* and a conditional allele of *Rbbp7* from MMRRC and the Wellcome Trust Sanger Institute respectively (**Fig. 3.2A) (**Skarnes et al., 2011). We found that loss of both *Rbbp4* alleles led to embryonic lethality prior to embryonic day 9 (0 embryos in 12 litters) consistent with data showing that loss of *Rbbp4* leads to severe developmental defects in pre-implantation embryos (Miao, Biol Repro 2020; Zhao, Epigenetics 2020).

Mice homozygous or hemizygous for the X-linked allele *Rbbp7*^{tm1a} were born in normal mendelian ratios, and analysis of RNA and protein from *Rbbp7*^{tm1a}/Y mice showed that the allele produces a functional isoform of *Rbbp7* which splices around the *LacZ* and *Neo* exons, and thus is unsuitable for studying loss-of-function (**Fig. 3.2B**). We also generated the *Rbbp7*^{LacZ} allele by crossing *Rbbp7*^{tm1a} *mice to beta-actin-Cre* mice. *LacZ* expression (X-Gal staining) matched the pattern of *Rbbp7* expression observed by ISH (**Fig. 3.2A, 3.2C**). Analysis of cDNA generated from this locus showed that it had multiple splice isoforms, including one encoding WT *Rbbp7*. We overcame this by generating a Cre-dependent conditional allele (*Rbbp7*^{Flox}) by recombination with *beta-actin FLP* mice (**Fig. 3.3A**). We used cell type specific Cre lines to conditionally delete *Rbbp7* using the *Rbbp7*^{Flox} allele in the developing BG and cortex.

Recombination of *Rbbp7*^{Flox} with *beta-actin-Cre* produces the constitutive null allele *Rbbp7*$^{\Delta E3}$ which lacks exon 3, leading to a frameshift and highly reduced amounts of RBBP7 protein (**Fig. 3.2B**). We observed that unlike the complete embryonic lethality observed in *Rbbp4* mutants, approximately 20% of the expected number of female *Rbbp7*$^{\Delta E3}$/*Rbbp7*$^{\Delta E3}$ mice progressed through embryogenesis and died at or before E17.5 (3 embryos in 10). Embryos which reached fetal stages were smaller than their wild type littermates and showed dilated blood vessels and hemorrhaging (**Fig. 3.2D)**. Viable *Rbbp7*$^{\Delta E3}$/Y mice were fertile and seemed phenotypically normal.

3B. Sensitized *Rbbp* knockout mice have reduced levels of mitosis in progenitors

Because viable *Rbbp7*$^{\Delta E3}$/Y mice did not have a clear telencephalic phenotype, we conditionally deleted the *Rbbp7*^{Flox} allele in a *Rbbp4*$^{+/-}$ background using either *Nkx2.1-Cre* (E9.5 MGE deletion; Xu et al., 2008) or *Emx1-Cre* (E10.5 cortex deletion; Guo et al, 2000) to reduce the total dosage of both RBBP proteins. In these experiments we also introduced the *Ai14* Cre reporter allele, which expresses tdTomato in cells which express CRE (Madisen et al., 2010) (**Fig. 3.3A**).

Rbbp4 $^{+/-}$*, Rbbp7* $^{Flox/Y}$, *Nkx2-1-Cre* embryos exhibited reduced MGE size and tdTomato+ ventricular surface area at E13.5 compared to control embryos (**Fig. 3.3B, 3.3C**). This altered morphology was accompanied by a decreased density in the number of mitotic phospho-Histone H3 (pH3) positive VZ cells in caudal planes of sections when normalized to pH3 density in the LGE, where *Nkx2-1-Cre* is not active (**Fig. 3.4A, 3.4B**). This reduction in the number of dividing cells in the caudal VZ at E13.5 is followed by a decrease in the size of the MGE VZ at E15.5 (**Fig. 3.4C**).

Conditional deletion of *Rbbp7* using *Emx1-Cre* yielded similar results. *Rbbp4*$^{+/-}$*, Rbbp7*$^{Flox/Y}$*, Emx1-Cre* animals had reduced cortical length, reduced thickness of the cortical plate

(CP), and an altered pattern of pH3 positive cells in the VZ compared with *Rbbp4*$^{+/-}$, *Rbbp7* $^{+/Y}$, *Emx1-Cre* littermates (**Fig. 3.5A-B**). We also observed small groupings of tdTomato+ cells approximately 20-60μm in diameter in mutant cortices, however the cause of these is unknown. These findings mirror the results of a conditional deletion of NuRD subunits *Hdac1* and *Hdac2* using *Emx1-Cre*, which also leads to decreased cortex thickness, reduced VZ proliferation, and a disorganization of cortical layers (Tang et al., 2019).

3C. Sensitized *Rbbp* knockout mice produce fewer cortical interneurons

Because the sensitized mutant had a reduction in cell proliferation in progenitors in the VZ, we also wanted to see if *Rbbp7* deletion had an impact on production of postmitotic cells derived from the MGE. We mapped the fate of tdTomato+ interneurons migrating to the cortex in two distinct regions: the superficial migratory stream (SMS) and deep migratory stream (DMS). Interneurons of the DMS travel through the SVZ of the LGE/Cortex, while interneurons of the SMS travel along the marginal zone (**Fig. 3.6A-C',** Marín and Rubenstein, 2001; Hernández-Miranda et al., 2010). We counted the density of interneurons in the DMS and SMS in *Rbbp4* $^{+/-}$ *Rbbp7* $^{Flox/Y}$ *Nkx2-1-Cre* from the ages of E13.5 to E16.5 and observed a larger reduction in overall numbers of interneurons at later ages, and especially in the deep migratory stream (**Fig. 3.6D, 3.6E**). By E16.5, mutants have very few tdTomato+ cells in VZ (<10 per section plane), suggesting that this reduction in interneuron production could be due to an exhaustion of the stem cell pool by this age.

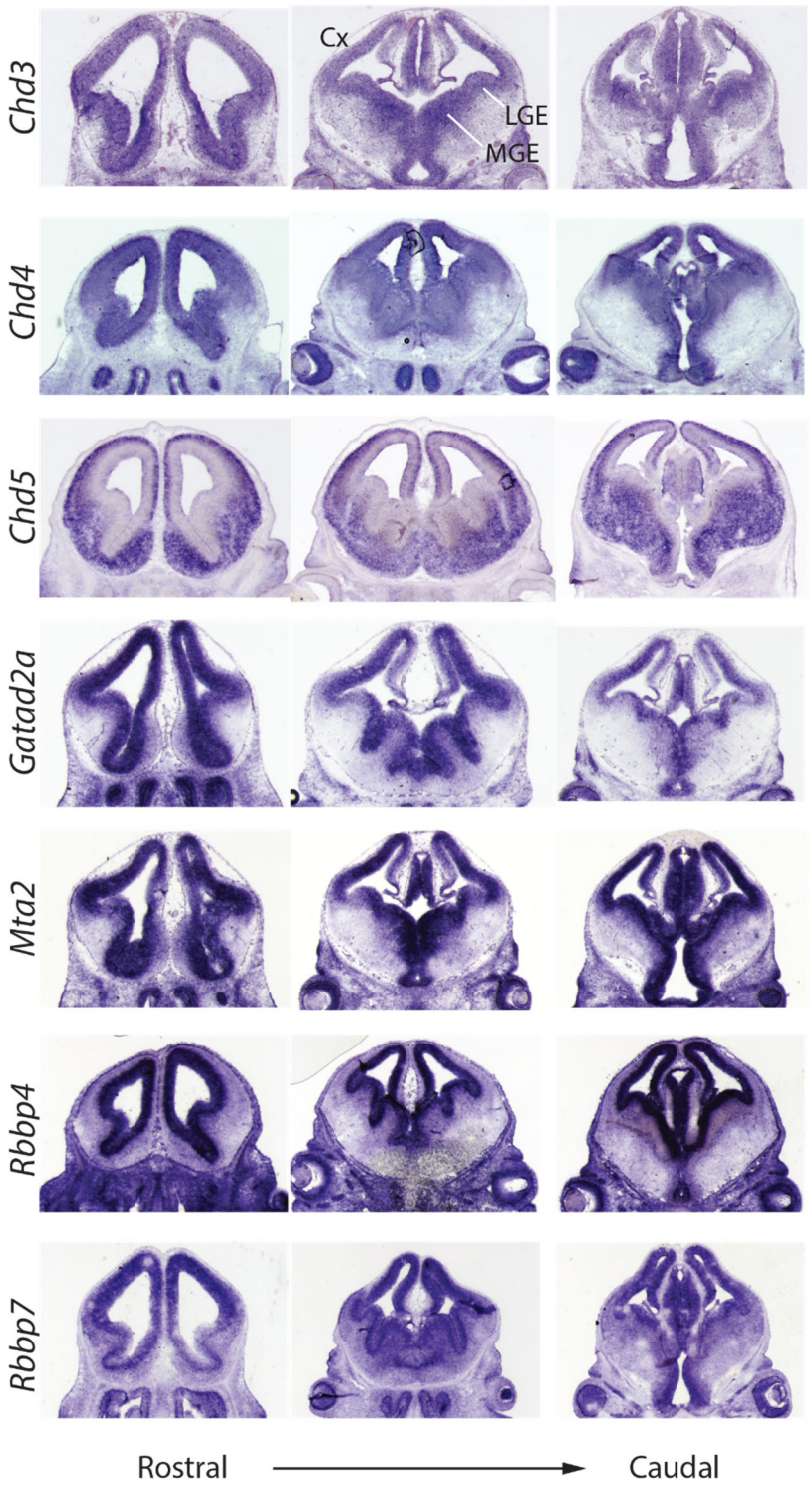

Figure 3.1: RNA expression of selected NuRD subunits at E13.5

RNA expression of NuRD subunits at E13.5 as assessed by *in situ* hybridization showing that all subunits except for *Chd5* are expressed in the BG at higher levels in the VZ&SVZ than in the MZ. Cx: cortex; LGE; lateral ganglionic eminence, MGE; medial ganglionic eminence.

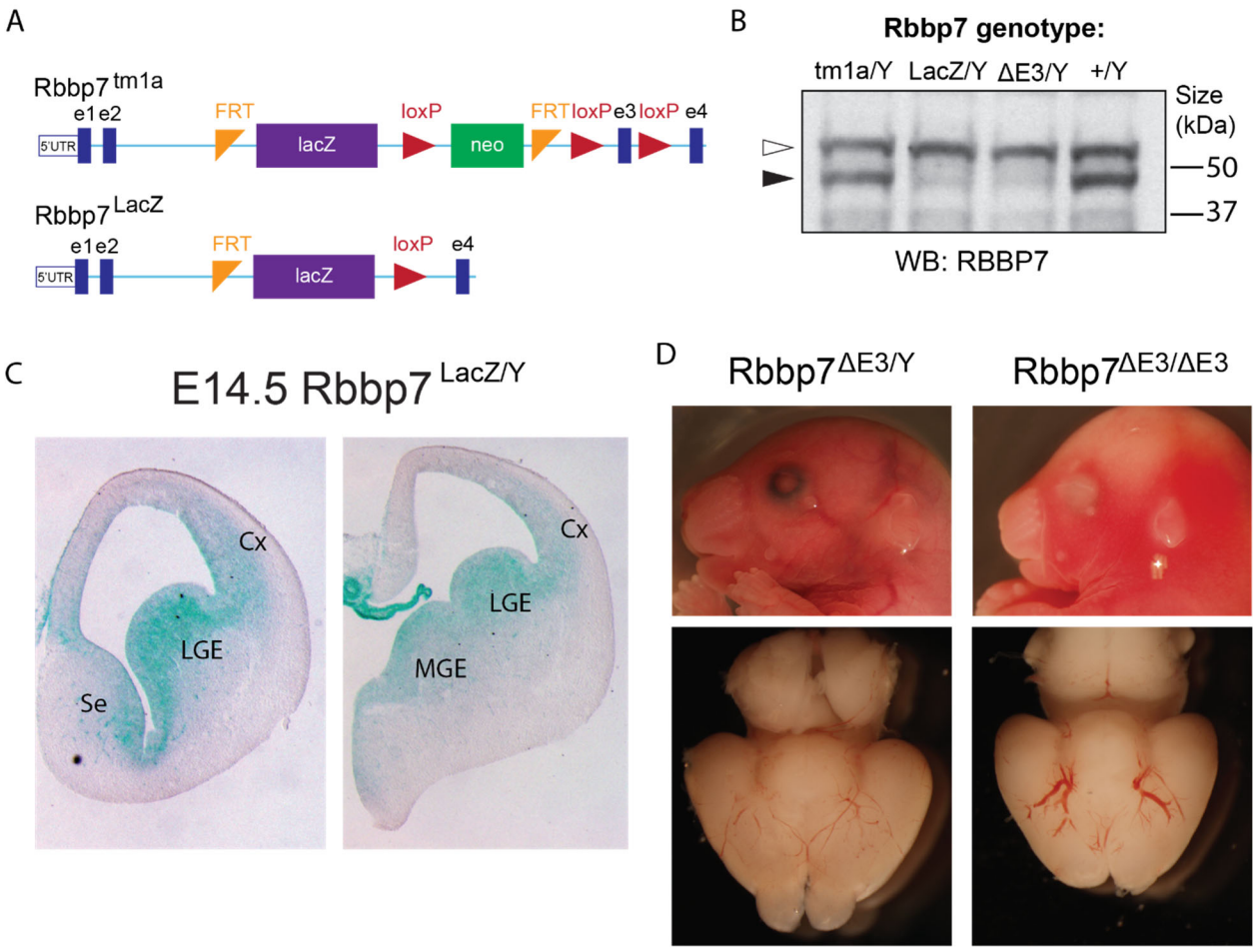

Figure 3.2: Homozygous deletion of exon 3 of *Rbbp7* leads to prenatal death and vascular abnormalities in females

A. Schematic of *Rbbp7*^{tm1a} and *Rbbp7*^{LacZ} knock-in transgenes. *Rbbp7*^{LacZ}, *Rbbp7*^{flox}, and *Rbbp7*$^{\Delta E3}$ loci are all derived from *Rbbp7*^{tm1a} by recombination with CRE and/or FLP. **B.** Western blot of RBBP7 from nuclear extracts derived from E13.5 mouse BG from mice with the four types of *Rbbp7* alleles. The *LacZ* and the *DE3* hemizygous mutants show a large reduction in a band at 46kDa (black arrow) corresponding to the RBBP7 protein. This antibody also recognizes a nonspecific with an apparent molecular weight of ~55kDa (white arrow). **C.** X-Gal staining of coronal sections from E14.5 *Rbbp7*$^{LacZ/Y}$ mutant showing the transgene is expressed primarily in the VZ and SVZ of the cortex (Cx), lateral ganglionic eminence (LGE), medial ganglionic eminence (MGE), and septum (Se). **D.** Lateral view of heads (top) and ventral view of dissected brains (bottom) of E16.5 *Rbbp7*$^{\Delta E3}$ mutant embryos. Female *Rbbp7*$^{\Delta E3/\ \Delta E3}$ embryos (right) displayed a hemorrhagic phenotype and enlarged ventral blood vessels, while male embryos (left) appear unaffected.

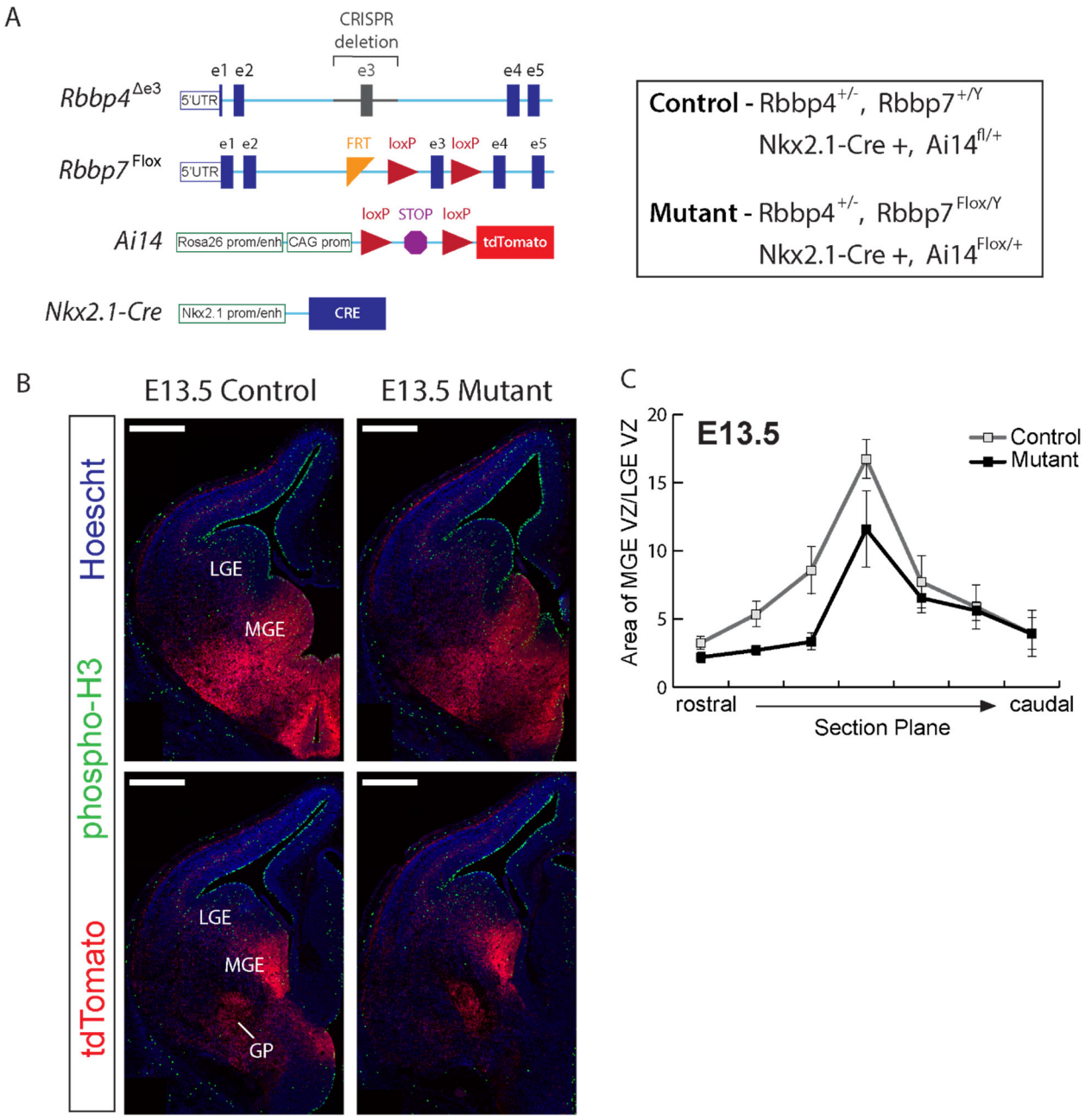

Figure 3.3: Reduction of RBBP4/7 leads to reduced rostral MGE size at E13.5

A. Schematic of genetic strategy for conditional (Cre) deletion of *Rbbp7* in the MGE of *Rbbp4*$^{+/-}$ (exon 3 deleted) embryos, with simultaneous fate mapping of *Nkx2.1* expressing cells using the *Ai14* tdTomato reporter. Full genotypes of mutants and control genotypes are explicitly described. **B.** Images of coronal sections from control and mutant brains at E13.5 showing tdTomato^{+} Nkx2-1-lineage cells. LGE: lateral ganglionic eminence, MGE: medial ganglionic eminence, VZ: ventricular zone, SVZ: subventricular zone, MZ: mantle zone, GP: globus pallidus. Scale bar: 500μm. **C.** Measurement of MGE VZ surface area normalized to LGE VZ surface area at E13.5, showing that the mutants have a reduced rostral MGE progenitor zone. Each measurement was performed at 7 planes of section (rostral-caudal, n=3).

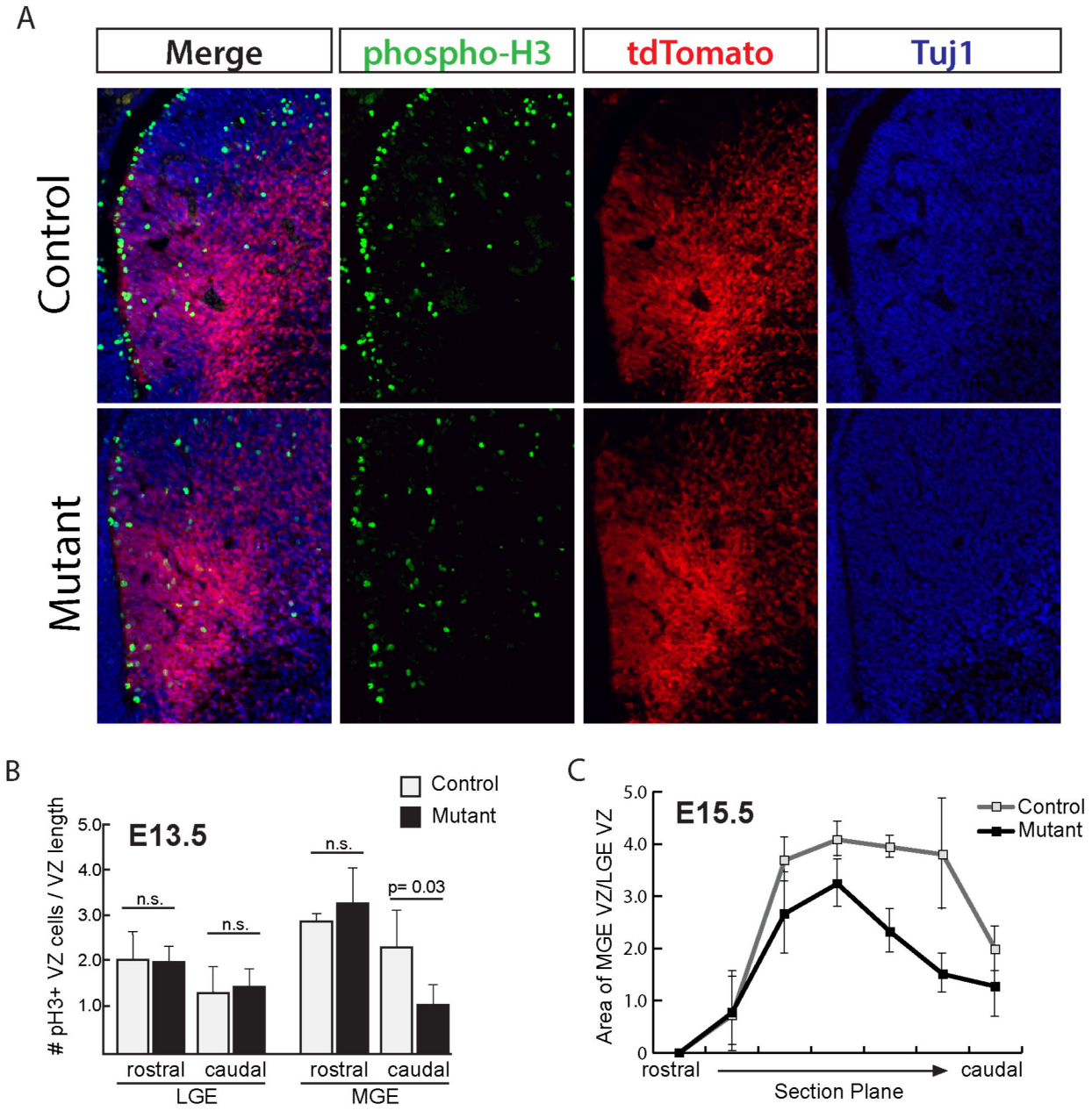

Figure 3.4: Reduced proliferation in mutants at E13.5 is followed by reduced MGE size at E15.5

A. Images of coronal sections from control and mutant brains at E13.5 showing immunostaining of phospho-Histone H3 (green), tdTomato lineage cells (red), and counterstained with Hoechst (blue). **B.** Quantification of the average number of phospho-Histone $H3^{+}$ cells in the VZ (normalized to VZ length) for the LGE and MGE in rostral and caudal planes of section at E13.5. Only the caudal MGE showed a significant reduction in the number of M-phase cells in the mutant compared to control. **C.** Measurement of MGE VZ surface area normalized to LGE VZ surface area at E15.5, showing that the mutants have a reduced caudal MGE progenitor zone. Each measurement was performed at 7 planes of section (rostral-caudal, n=3).

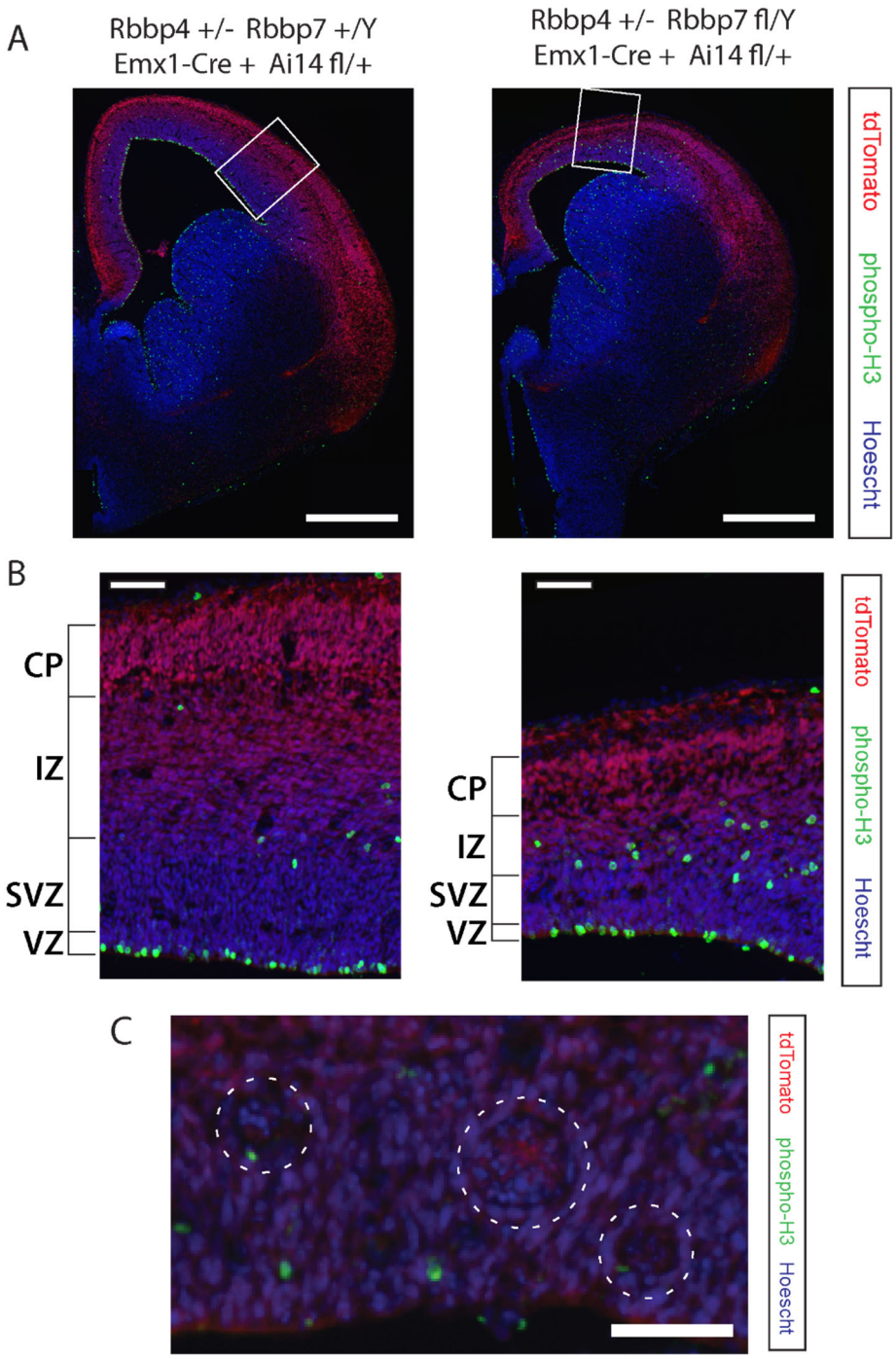

Figure 3.5. Reduction of RBBP4/7 by *Emx1-Cre* leads to cortical defects

A. Images from coronal sections of the cortex from control (left) and mutant (right) brains at E13.5 showing immunostaining for phospho-Histone H3 (green), tdTomato lineage cells (red), and counterstained with Hoechst (blue). Scale bar: 500μm **B.** High magnification images of insets from panel A showing an altered pattern of phospho-Histone H3 cells in VZ and SVZ of mutant brain. Scale bar: 50μm **C.** Abnormal tdTomato+ circular groupings of cells are present in mutant, but not control cortices. Scale bar : 50μm.

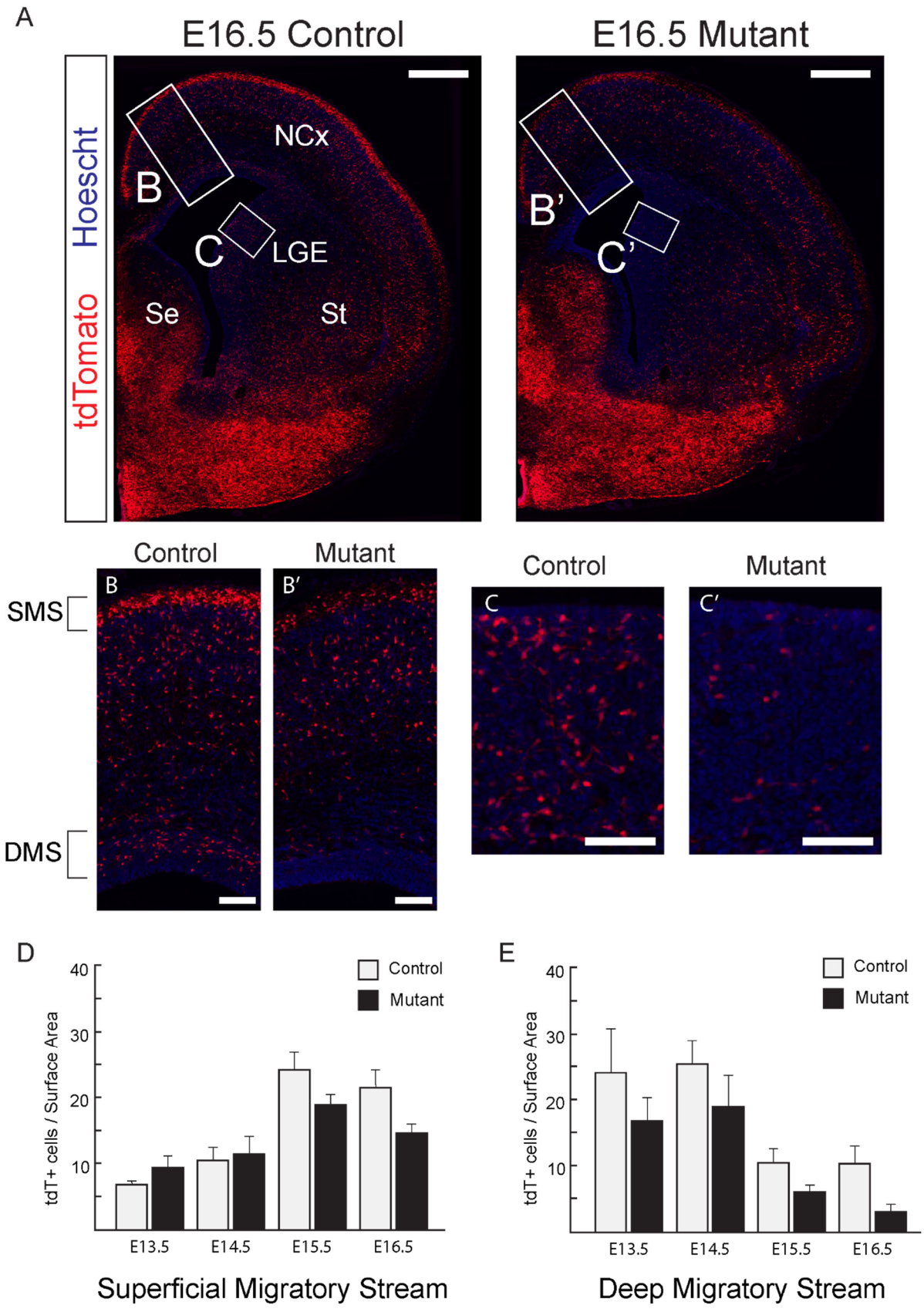
A
E16.5 Control
E16.5 Mutant
Hoescht
tdTomato
NCx
B
C
LGE
Se
St
B'
C'
Control
Mutant
SMS
DMS
B
B'
C
C'
D
E
Control
Mutant
tdT+ cells / Surface Area
40
30
20
10
E13.5
E14.5
E15.5
E16.5
Superficial Migratory Stream
Deep Migratory Stream

Figure 3.6. Reduction of RBBP4/7 leads to reduced numbers of cortical interneurons

A. Images from coronal sections of control and *Rbbp4/Rbbp7* mutant brains at E16.5 showing a reduction of MGE-derived tdTomato positive cells in the cortex and LGE. Boxes B (cortex) and D (LGE progenitor zones) are shown below. Scale bar: 500um. **B, B'.** Higher magnification images of insets from panel A showing reduced numbers of MGE-derived tdTomato positive cells in the cortex. SMS: superficial migratory stream, DMS: deep migratory stream. Scale bar: 100um. **C, C'.** Higher magnification images of insets from panel A showing reduced numbers of MGE-derived tdTomato positive cells in the progenitor zone of the LGE. **D, E.** Quantification of cortical interneurons ($tdTomato^+$ cells/area) in controls and *Rbbp4*/7 mutants in the superficial (**D**) and deep (**E**) migratory streams from 7 planes of section each. The mutants showed the largest reduction in interneuron density at E16.5. n=1 embryo for each age and genotype, 7 planes of section for each.

Chapter 4

DLX1 and NuRD bind a common set of putative regulatory elements

4A. DLX1 and NuRD share a common set of bound genomic loci

Since RBBP4/7 interact with DLX1 *in vitro* and *in vivo*, we hypothesized that DLX1 may assist in stabilization and/or recruitment of the NuRD complex to chromosomal regulatory loci critical for subpallial development. We therefore profiled the genome occupancy of several key members of the NuRD complex in the E13.5 subpallium using chromatin immunoprecipitation sequencing (ChIP-seq) with antibodies to CHD4, HDAC1, HDAC2, MBD3, RBBP4 and RBBP7. Additionally, we performed the Assay for Transposase-Accessible Chromatin sequencing (ATAC-seq) in E13.5 BG tissue to measure levels of chromatin accessibility throughout the genome. The basic characteristics of these data sets are described in **Table 4.1**.

We compared the binding profiles of each of these experiments across the entire genome and observed a high degree of correlation between all NuRD complex subunits, with the strongest correlations occurring between CHD4, MBD3, HDAC2, and RBBP4 (Spearman correlation coefficient >0.84) (**Fig. 4.1A**). RBBP4 is known to associate with the PRC2 repressive complex (Kuzmichev et al., 2002), however RBBP4 ChIP-seq was more closely correlated with H3K27ac and to regions of accessible chromatin, than to H3K27me3. This pattern was also true for ChIP-seq of other NuRD members (**Fig. 4.1A**). This finding may be explained by an *in vitro* study by Millard et al. 2016 which demonstrated that RBBP4, either alone or complexed with MTA2, has a higher binding affinity for H3K27ac than H3K27me3.

DLX TF ChIP-seq peaks were found primarily at intronic and intergenic loci, while a higher proportion of NuRD subunit ChIP-seq peaks were within 2kb of a transcription start site (TSS) (**Fig. 4.1B, 4.1D**). Despite this difference in binding patterns, many loci bound by DLX1 were also bound by NuRD subunits; the correlation coefficient between RBBP4 and DLX1 was similar to that as between DLX1 and DLX2 (0.72 for RBBP4 vs. 0.75 for DLX2). In fact, more than half of loci bound by DLX1 were also bound by RBBP4 (4429/8002 DLX1 peaks).

We performed motif enrichment analysis of RBBP4 ChIP peaks and found that the five motifs with the smallest p-values in both datasets contained the core homeobox sequence TAATTA flanked by C/G (**Fig. 4.1C**). These motifs closely resemble the consensus DLX1 and DLX2 binding motifs (Lindtner et al., 2019; Feledy et al., 1999).

4B. NuRD and DLX1 co-bound loci are enriched near transcription factor genes

We defined a high-confidence (HC) dataset of NuRD binding, by intersecting the CHD4, HDAC1/2, MBD3, and RBBP4/7 data sets. This had 2,921 peaks which we termed HC-NuRD. Because the presence of HDAC1/2 and RBBP4/7 is variable within the NuRD complex (Millard et al., 2016; Low et al., 2020), we used the unions of RBBP4/7 and HDAC1/2 in the HC-NuRD data set. These 2,921 peaks represent <10% of loci bound by RBBP4, however HC-NuRD peaks represent more than half of the CHD4 dataset, which had the fewest called regions at 5,517.

HC-NuRD peaks were found primarily at promoters, with a smaller fraction bound to intronic and intergenic loci (**Fig. 4.1B**). We used K-means clustering to separate HC-NuRD peaks into three groups based on H3K27ac, H3K27me3 and DLX1 occupancy (**Fig. 4.2A**). Cluster 1 (C1) regions had the highest levels of both RBBP4 and DLX1 signal. They also exhibited a bimodal distribution of H3K27ac, with low H3K27me3, a pattern characteristic of intergenic regulatory elements. Consistent with this, 85% of C1 peaks were intronic or intergenic loci (**Fig. 4.2B**). By contrast, Cluster 2 and 3 (C2 and C3) peaks were primarily located within 5kb of the nearest TSS**.** Gene ontology of C1 peaks was enriched for the terms “DNA-templated transcription” and “nucleic acid-templated transcription”, notable since these terms are not significantly enriched in either DLX1 or HC-NuRD peaks alone (**Fig. 4.2C**). Many genes associated with these terms are TFs whose expression is altered in *Dlx1/2* $^{-/-}$ mutants. These include genes that have increased (e.g. *Otx2*, *Sall3*) or decreased (e.g. *Arx*, *Sp8*) expression in *Dlx1/2* $^{-/-}$ mutants measured by ISH and/or RNAseq (Long et al., 2009; Lindtner et al., 2019).

Table 4.1: Basic Characteristics of ChIP-seq datasets used in this study

Experiment	Age	Tissue Type	Sequencing Type	# of reads	# of called peaks	Reference
CHD4	E13.5	whole ganglionic eminences (BG)	SE50	46,088,058	5,517	
DLX1	E13.5	whole ganglionic eminences (BG)	SE50	51,379,299	8,000	Lindtner et al. 2019
DLX2	E13.5	whole ganglionic eminences (BG)	SE50	48,224,881	15,832	Lindtner et al. 2019
H3K27ac	E13.5	whole ganglionic eminences (BG)	SE50	47,563,650	289,604	Lindtner et al. 2019
H3K27me3	E13.5	whole ganglionic eminences (BG)	SE50	52,066,294	192,530	Lindtner et al. 2019
HC-NuRD	E13.5	whole ganglionic eminences (BG)	SE50	n/a	2,921	
HDAC1	E13.5	whole ganglionic eminences (BG)	SE50	30,051,949	18,274	
HDAC2	E13.5	whole ganglionic eminences (BG)	SE50	19,862,089	11,288	
MBD3	E13.5	whole ganglionic eminences (BG)	SE50	31,960,654	11,721	
RBBP4	E13.5	whole ganglionic eminences (BG)	SE50	40,960,759	29,762	
RBBP7	E13.5	whole ganglionic eminences (BG)	SE50	10,272,624	14,918	
ATAC-seq	E13.5	whole ganglionic eminences (BG)	PE 100	5,270,856	17,378	

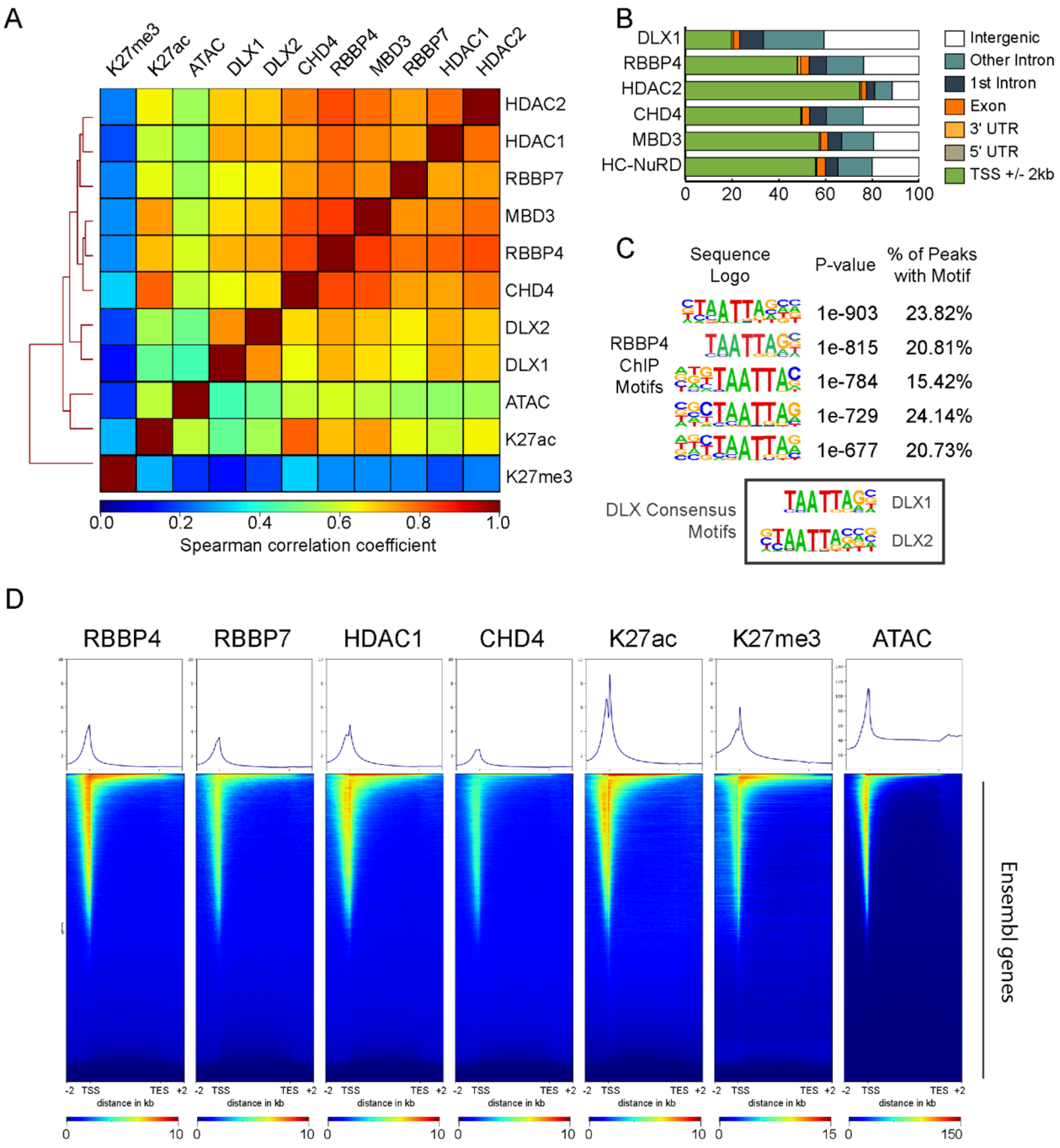

Figure 4.1: DLX1 and the NuRD complex co-occupy sites throughout the genome

A. Heatmap of pairwise Spearman correlation coefficients among ATAC-seq and ChIP-seq experiments from E13.5 BG tissue. The dendrogram on the left indicates which samples' read counts are most similar. K27me3: Histone H3K27 trimethyl, and K27ac: Histone H3K27 acetyl. **B.** Genomic distribution of called peaks for selected ChIP-seq experiments. TSS: transcription start site, UTR: untranslated region, HC-NuRD: high confidence NuRD peaks. **C.** Most significantly enriched DNA motifs identified in RBBP4 ChIP-seq peaks, all of which contain the core homeobox

sequence TAATTA. The top two motifs closely resemble the consensus binding motifs for DLX1 and DLX2. **D.** Heatmap representing peak height at all Ensembl and flanking 2kb upstream of TSS and downstream of TES. TSS: transcription start site, TES: transcription end site.

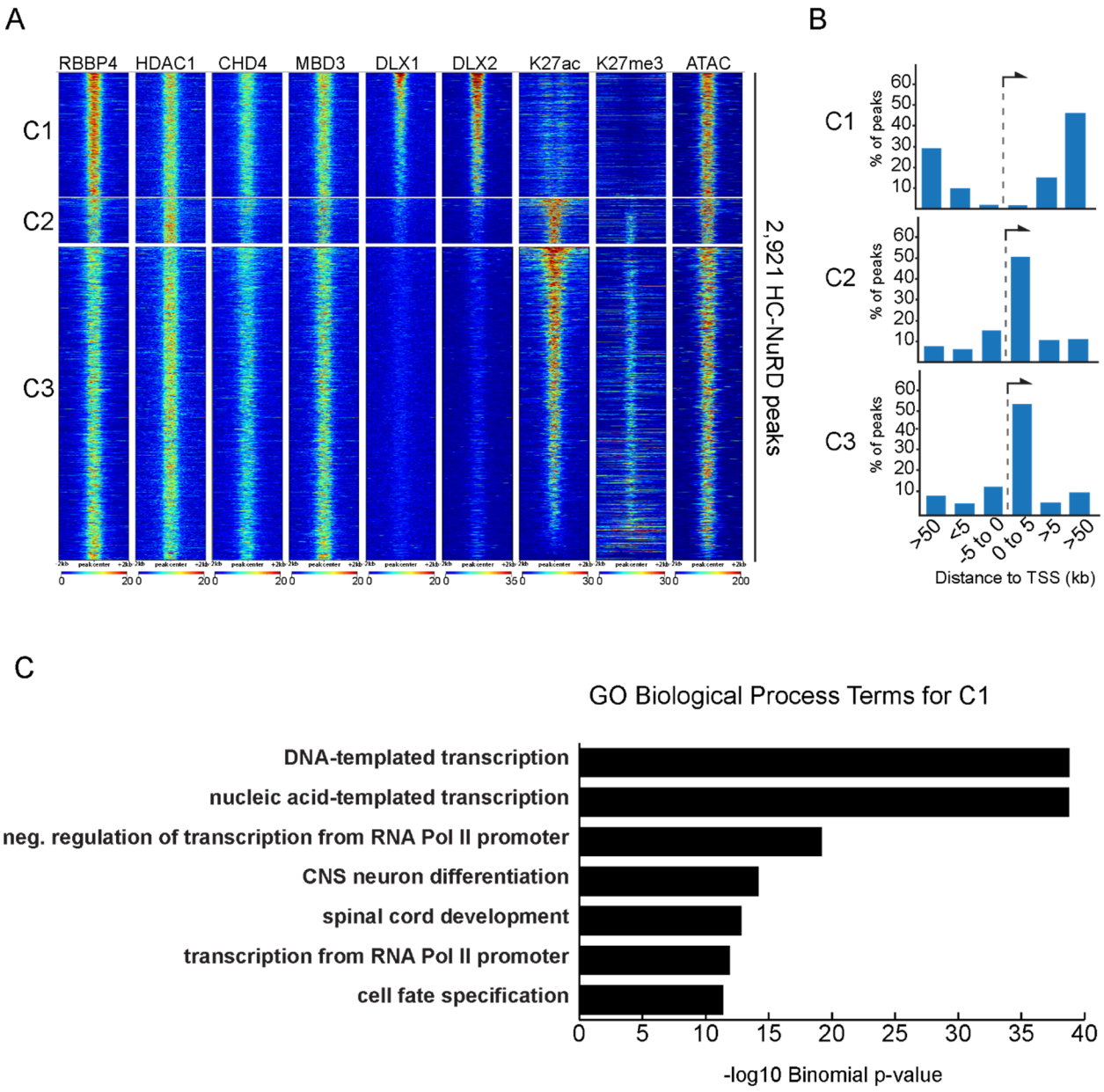

Figure 4.2: Loci co-bound by DLX1 and NuRD are pREs near transcription factors

A. Heatmap representing peak height of 2,921 HC-NuRD peaks separated into three groups by k-means clustering: C1, C2, and C3. C1 peaks have the highest signal enrichment for RBBP4, DLX1, and DLX2 and lowest enrichment for H3K27me3. **B.** Distance of peaks from the three clusters from panel D to transcription start site of the nearest gene as a percentage of the total peaks from each cluster. C1 peaks are primarily intronic and intergenic, while C2 and C3 peaks are enriched near promoters. **C.** Top Biological Process Gene Ontology terms of C1 HC-NuRD peaks from panels A&B as ranked by -$\log_{10}$ p-value.

Chapter 5

Loss of *Dlx1/2* leads to increased genomic accessibility and transcriptional derepression of *Olig2*

5A. NuRD and DLX1 bind to genomic loci which are decommissioned during development

Mice lacking *Dlx1* exhibit only subtle phenotypes due to a compensatory effect of *Dlx2*, whereas homozygous loss of *Dlx1/2* leads to the upregulation and ectopic expression of genes which are normally restricted to the VZ (Long et al., 2009). Many of the genes that are repressed by DLX TFs have evidence of DLX1 and DLX2 binding at nearby intergenic putative REs (pREs) (Lindtner et al., 2019). Because we find that DLX1 and the NuRD complex co-localize in the VZ/SVZ1 and co-bind approximately 2,000 genomic loci, we hypothesized that DLX1 may repress gene expression by recruiting the nucleosome remodeling and histone deacetylase activity of the NuRD complex to the appropriate pREs.

We have observed changes in the levels of H3K27ac at pREs in *Dlx1/2* mutant mice but have not yet observed whether loss of *Dlx1/2* impacts chromatin accessibility (Lindtner et al., 2019). To test this, we isolated populations of VZ and SVZ/MZ cells from the E13.5 BG of 3 WT and 3 *Dlx1/2* $^{-/-}$ embryos using the FlashTag method (Govindan et al, 2018). We then performed ATAC-seq from these purified populations to measure changes in chromatin accessibility as cells of the VZ mature to SVZ/MZ cells (**Fig. 5.1A**). The dendrogram of pairwise correlations between ATAC-seq samples showed that the SVZ/MZ *Dlx1/2*$^{-/-}$ samples clustered separately from the WT samples, while clustering of VZ samples clustered without regard to genotype (**Fig. 5.1B**). We observed that the mean ATAC-seq signal at regions bound by DLX1 were nearly identical between WT and *Dlx1/2* $^{-/-}$ in the VZ, however we observed an increase in ATAC-seq signal intensity in *Dlx1/2* $^{-/-}$ SVZ/MZ samples (**Fig. 5.1C**). WT and *Dlx1/2* $^{-/-}$ VZ had very few genomic loci with significant ($p < 0.01$) changes in ATAC-seq signal. On the other hand, the mutant SVZ/MZ had 1,910 regions with increased ATAC-seq signal (increased genomic accessibility) compared to WT (**Fig. 5.2A**). The majority of these regions begin as accessible in the WT VZ but have reduced accessibility in the WT SVZ/MZ. In *Dlx1/2* $^{-/-}$ embryos, however, these regions retain accessibility and fail to be decommissioned in *Dlx1/2*$^{-/-}$ SVZ/MZ samples, leading us to term these

regions “Not Decommissioned in Mutant”, or NDIM (**Fig. 5.2B**). Similar to the regions bound by DLX1, these 1,910 regions were primarily intergenic and intronic pREs (**Fig. 5.2C**). Analysis of neighboring genes found that they were enriched for terms associated with both neurogenesis and gliogenesis (**Fig. 5.2D**).

To see whether NDIM peaks were associated with transcriptional repression, we looked at changes in chromatin accessibility near 31 genes which have high expression in the VZ or SVZ of the BG at E13.5 and are known to have altered expression in *Dlx1/2* mutants. We found that NDIM peaks were primarily near BG genes whose expression is upregulated or ectopically expressed in the *Dlx1/2* $^{-/-}$ mutant (**Table 5.1**). This is especially true of NDIM peaks bound by NuRD (HC-NuRD) and DLX1. One of these NDIM peaks overlapped with the VISTA enhancer mm817 which is upstream of *Olig2*, an enhancer with forebrain activity at E11.5 (**Fig. 5.3A, 5.3B**).

5B. Co-Heterozygosity of *Rbbp4* and *Dlx1/2* leads to upregulation of *Olig2* expression

Dlx1/2 and *Olig1/2* have a mutually repressive relationship. It is known that OLIG1 binds to the i12b RE within the *Dlx1/2* bigene cluster, however the specific molecular mechanism by which DLX TFs repress *Olig1/2* is unknown (Silbereis et al., 2014). Because mm817 exhibits altered chromatin accessibility and is bound by DLX1 and NuRD complex subunits, we hypothesized that NuRD and DLX1 together repress transcription at the *Olig1/2* locus. A corollary of this hypothesis is that one can reproduce a similar phenotype as in *Dlx1/2*$^{-/-}$ animals by reducing the dosage of NuRD components, such as *Rbbp4*. Thus, we crossed *Dlx1/2* $^{+/-}$ and *Rbbp4* $^{+/-}$ mice to attenuate the levels of both and examined the numbers of OLIG2^{+} cells in the neonatal SVZ, a region which expresses *Dlx1/2* (Alvarez-Buylla and Lim, 2004). We observed a significant increase in the density of OLIG2^{+} cells in both the septal and striatal SVZ in *Dlx1/2* $^{+/-}$ *Rbbp4* $^{+/-}$ animals, but not in *Dlx1/2* $^{+/-}$ animals, at postnatal day 5 (P5) (**Fig. 5.3C-E**). This provides evidence that *Dlx1/2* and *Rppb4* (and likely the NuRD complex) function together to repress *Olig2* and the fate balance between neurons and glia.

Table 5.1: Number of peaks with ATAC-seq enrichment in SVZ/MZ near *Dlx*-regulated genes

VZ Genes

	WT	*Dlx1/2*$^{-/-}$ (NDIM)	NDIM +DLX1 +NuRD
Ascl1	0	2	1
* Gbx1	0	0	0
* Gbx2	0	2	1
Gsx2	0	1	1
Nkx2-1	0	3	0
Nr2f1	0	2	0
Olig1	0	1	0
Olig2	0	1	1
Otx2	0	3	0
Six3	1	4	0
Sp9	0	1	0
Tox	0	1	0
Zbtb20	0	2	0

SVZ Genes

	WT	*Dlx1/2*$^{-/-}$ (NDIM)	NDIM +DLX1 +NuRD
* Ebf3	0	3	0
* Gsx1	0	2	0
* Id2	0	2	0
Isl1	0	10	2
* Pax7	0	2	0
Prokr2	0	1	0
* Otp	0	1	0
Dlx5	5	0	0
Dlx6	15	0	0
Drd2	0	0	0
Erbb4	0	1	0
Lhx6	0	0	0
Lhx8	1	1	0
Mafb	0	1	0
Pou3f4	0	0	0
Slc32a1	4	0	0
Sp8	0	1	0
Vax1	0	0	0
Zfhx3	0	3	0

Number of called peaks with differential enrichment in E13.5 ATAC-seq near genes which are upregulated (pink highlight) or downregulated (green highlight) in the *Dlx1/2*$^{-/-}$ mutant. Genes are separated based on whether their normal expression is highest in the VZ (left) or SVZ (right). Genes with an asterisk are ectopically expressed in the mutant. Column headings indicate peaks of the following criteria- WT: enriched in WT SVZ/MZ samples vs. *Dlx1/2*$^{-/-}$ SVZ/MZ; *Dlx1/2*$^{-/-}$ (NDIM): enriched in *Dlx1/2*$^{-/-}$ SVZ/MZ vs. WT SVZ/MZ samples; NDIM+DLX1+NuRD: NDIM peaks which also have called peaks in DLX1 and HC-NuRD ChIP-seq datasets.

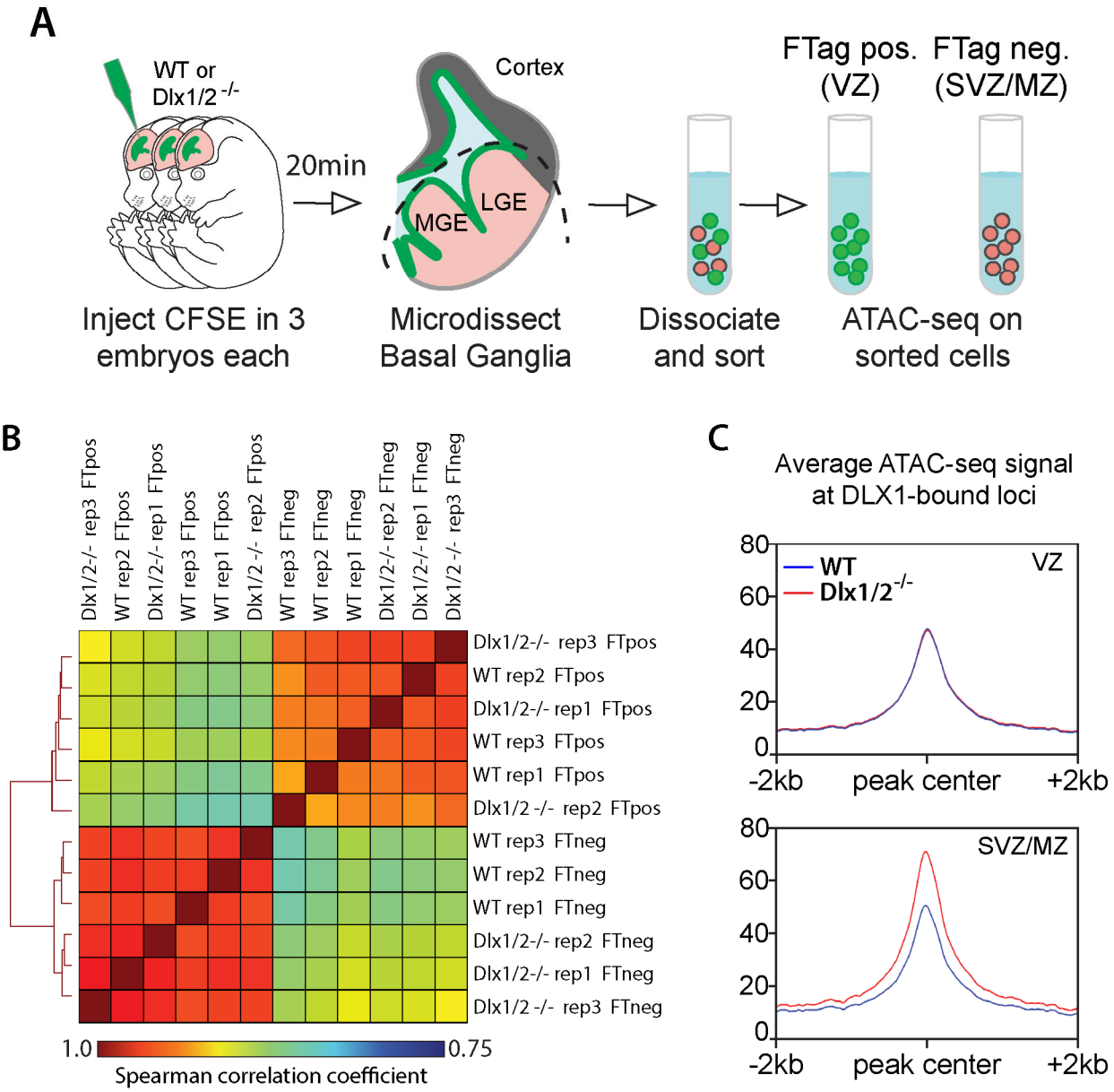

Figure 5.1: Loss of *Dlx1/2* leads to decreased chromatin accessibility at DLX1-bound loci

A. Design of experiment to identify ATAC-seq peaks in the VZ and SVZ/MZ in WT and *Dlx1/2*$^{-/-}$ E12.5 BG. Fluorescent CFSE dye was injected into the lateral ventricles of 3 WT and 3 *Dlx1/2*$^{-/-}$ embryos to label ventricular-contacting (VZ) cells, while leaving subventricular and mantle zone (SVZ/MZ) cells unlabeled. BG cells were dissociated and purified using FACS. 50,000 cells were collected from both CFSE-positive and CFSE-negative populations and ATAC-seq was then performed on each. **B.** Heatmap of pairwise Spearman correlation coefficients among individual ATAC-seq replicates from purified populations of E12.5 BG cells. The dendrogram on the left indicates which samples' read counts are most similar. All VZ samples (FTpos) form a single cluster, but SVZ/MZ samples (FTneg) cluster according to genotype. **C.** Mean ATAC-seq signal intensity from labeled (VZ, left panel) and unlabeled (SVZ/MZ, right panel) cells of each genotype at DLX1 called peaks.

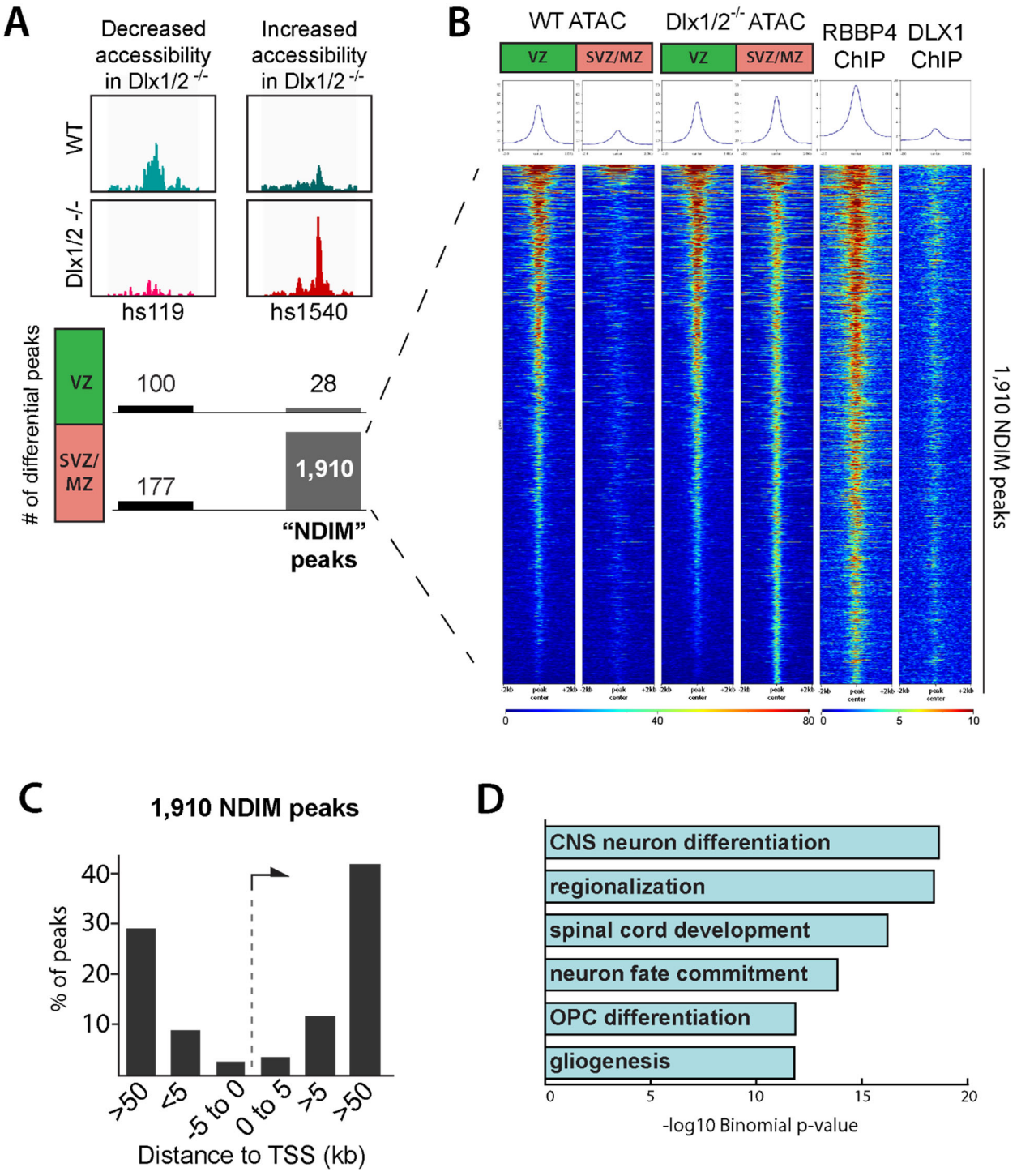

Figure 5.2: A subset of decommissioned pREs retain accessibility in the SVZ of *Dlx1/2* mutants

A. Top: ATAC-seq peaks from intergenic peaks nearby *Arx* and *Ascl1* in WT (top, teal) or *Dlx1/2*$^{-/-}$ (bottom, red*);* these loci have either decreased (left) or increased (right) accessibility in *Dlx1/2*$^{-/-}$*.* These loci are also VISTA enhancers (hs119 and hs1540) with telencephalic activity. Bottom: Number of peaks identified as having increased or decreased ATAC-seq accessibility in *Dlx1/2*$^{-/-}$ VZ (green, top) or SVZ/MZ (pink, bottom) samples using a p-value of 0.01. NDIM peaks:

not decommissioned in the *Dlx1/2*$^{-/-}$ mutant. **B.** Heatmap of ATAC-seq signal in VZ and SVZ/MZ samples of WT and *Dlx1/2*$^{-/-}$ samples, and ChIP-seq signal of RBBP4 and DLX1 WT ChIP at NDIM peaks with 2kb flanking either side of the peak. Mean peak intensity across all regions is plotted above heatmaps. NDIM peaks generally have similar ATAC-seq signal in VZ samples of both genotypes but fail to be decommissioned in *Dlx1/2*$^{-/-}$ SVZ/MZ. **C.** Distance of the 1,910 NDIM peaks to transcription start site of the nearest gene as a percentage of total peaks. **D.** Top Biological Process Gene Ontology terms of 1,910 NDIM peaks from panels C-E as ranked by -$\log_{10}$ p-value.

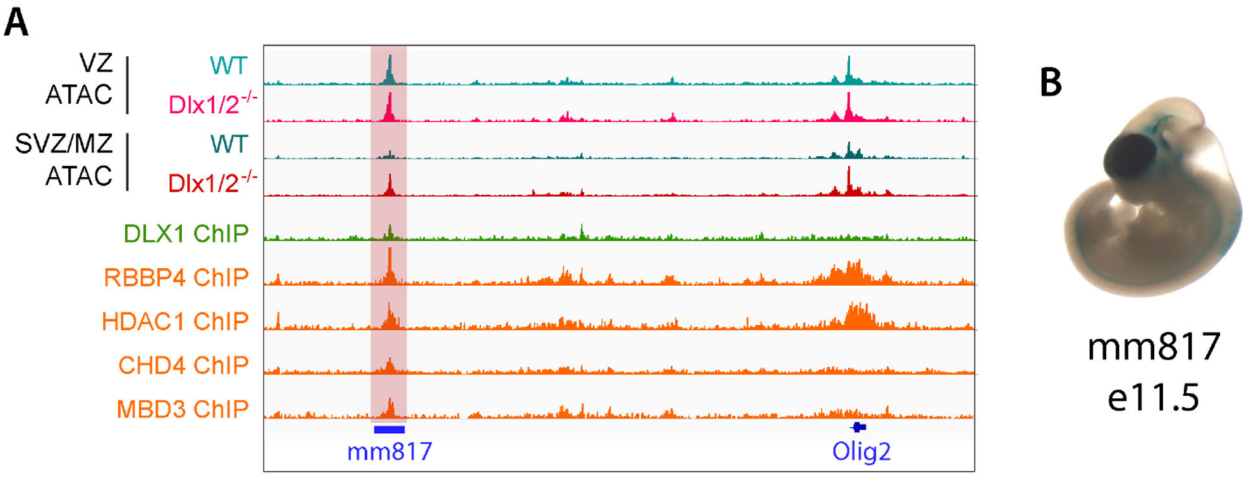
A
VZ ATAC
WT
Dlx1/2-/-
SVZ/MZ ATAC
WT
Dlx1/2-/-
DLX1 ChIP
RBBP4 ChIP
HDAC1 ChIP
CHD4 ChIP
MBD3 ChIP
mm817
Olig2
B
mm817
e11.5

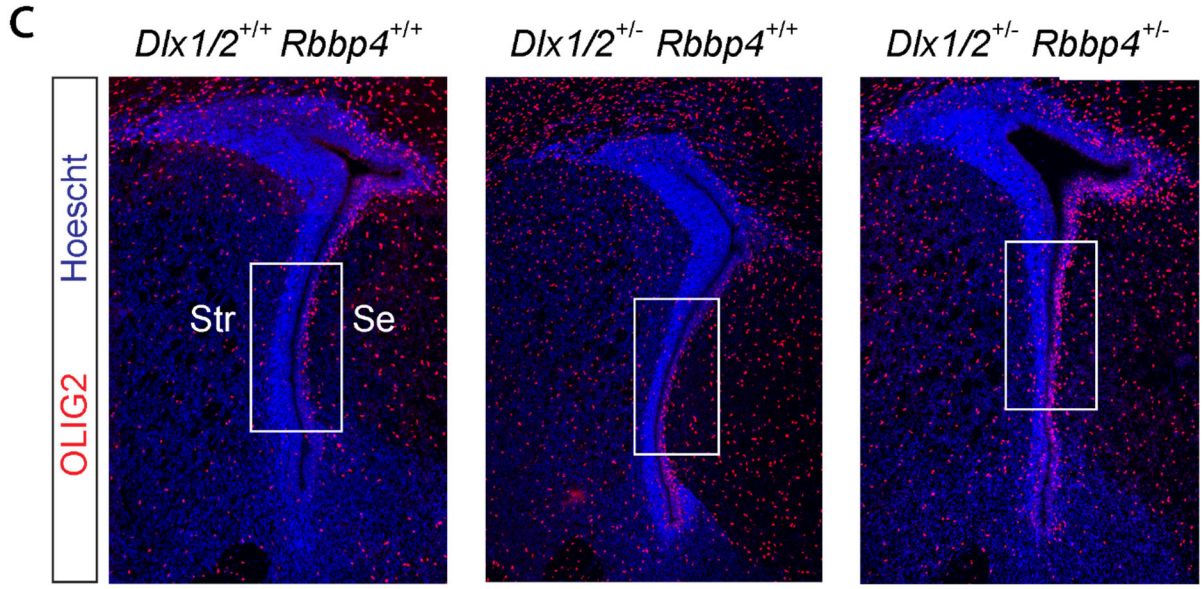
C
Dlx1/2+/+ Rbbp4+/+
Dlx1/2+/- Rbbp4+/+
Dlx1/2+/- Rbbp4+/-
Hoescht
OLIG2
Str
Se

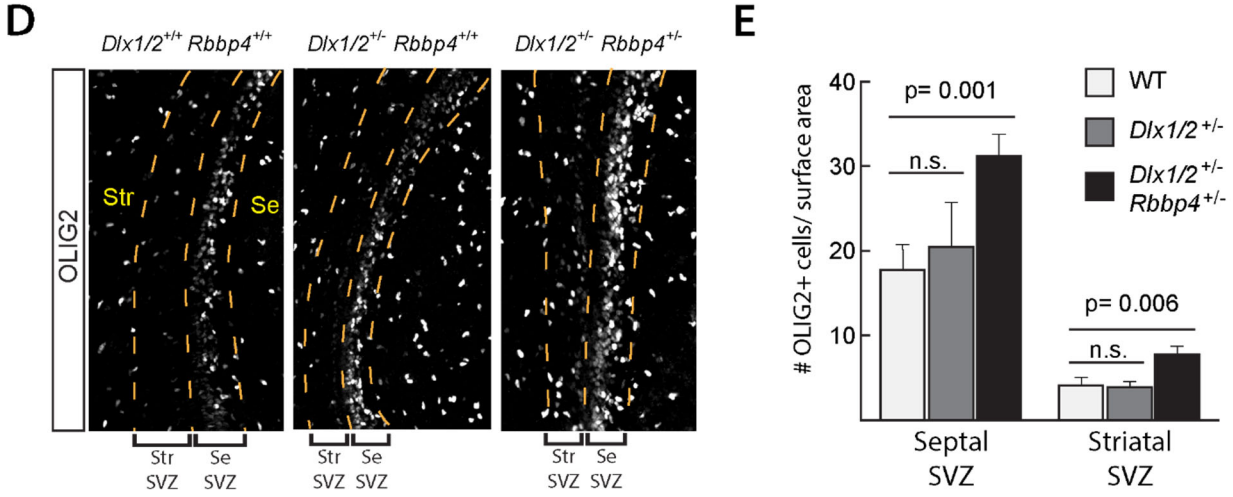
D
Dlx1/2+/+ Rbbp4+/+
Dlx1/2+/- Rbbp4+/+
Dlx1/2+/- Rbbp4+/-
OLIG2
Str
Se
Str SVZ
Se SVZ
E
OLIG2+ cells/ surface area
40
30
20
10
p= 0.001
n.s.
p= 0.006
n.s.
WT
Dlx1/2+/-
Dlx1/2+/- Rbbp4+/-
Septal SVZ
Striatal SVZ

Figure 5.3: Reduction in both *Dlx1/2* and *Rbbp4* dosage leads to increased OLIG2 expression in the neonatal telencephalic SVZ

A. Genomic tracks showing the mean ATAC-seq signal intensity of the three replicates of ATAC-seq from FlashTag positive (VZ) and negative (SVZ/MZ) cells derived from E12.5 WT and *Dlx1/2*$^{-/-}$ BG. Also pictured is ChIP-seq from E13.5 WT BG. Region highlighted in pink is a distal pRE (VISTA enhancer mm817) near *Olig2* which is an NDIM, DLX1, and HC-NuRD called peak. **B.** Wholemount X-Gal staining VISTA enhancer mm817 demonstrates telencephalic activity at E11.5. **C.** Immunostaining for OLIG2 (red) counterstained with Hoechst (blue) on telencephalic coronal sections of postnatal day 5 WT (left), *Dlx1/2*$^{+/-}$(center), and *Dlx1/2*$^{+/-}$*, Rbbp4*$^{+/-}$ (right) mice showing an increase in the number of OLIG^{+} cells in SVZ of the subpallial Septum (Se) and to a lesser degree in the Striatum (Str). **D.** High magnification of OLIG2 immunostaining from boxed region of panel A. Striatal and Septal SVZ are indicated below. **E.** Quantification of OLIG2^{+} cells from 6 images each from WT, *Dlx1/2*$^{+/-}$, or *Dlx1/2*$^{+/-}$*, Rbbp4*$^{+/-}$ brains at P5. n=3.

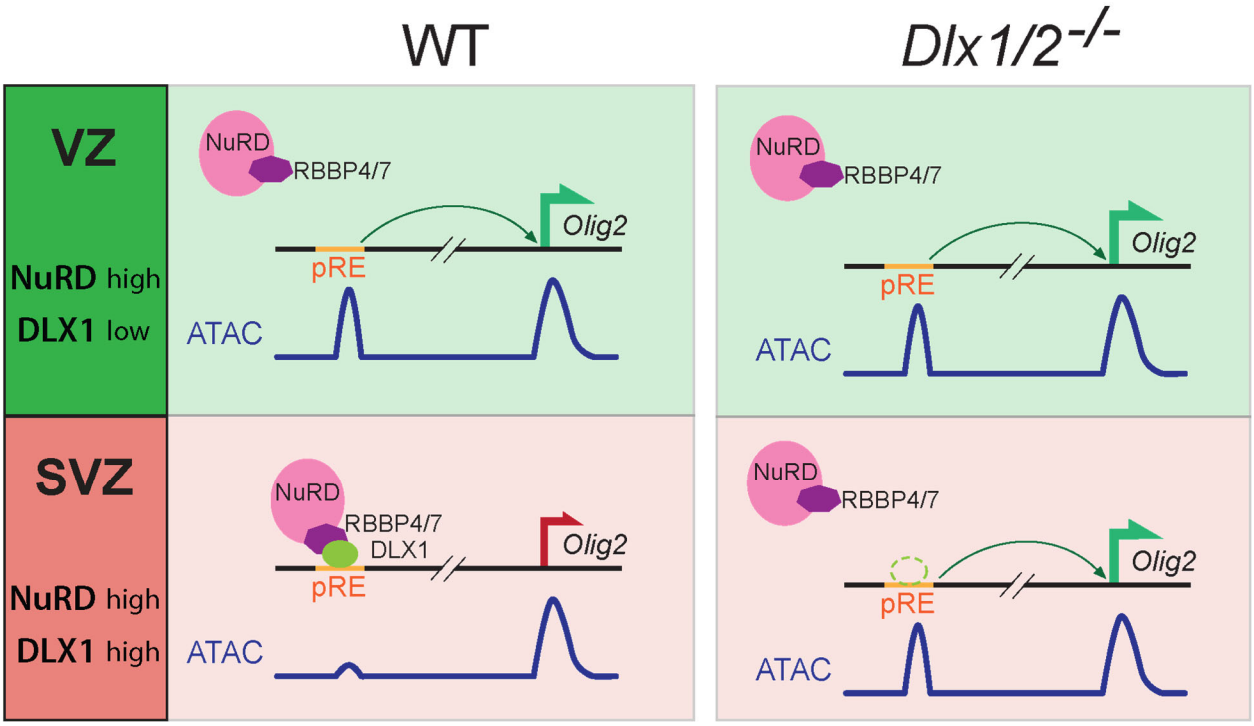

Figure 5.4: Proposed Model for DLX1-mediated gene repression

REs near VZ genes such as *Olig2* have an open chromatin state in VZ cells. As cells differentiate and migrate to the SVZ, they upregulate *Dlx1* expression. DLX1 binds to these REs and recruits NuRD through an interaction with RBBP4/7, leading to a decrease in chromatin accessibility and transcription of target genes. In the absence of DLX1/2, these regions remain accessible, leading to an increase in SVZ expression of associated gene(s).

Chapter 6

Discussion of Major Findings

DLX TFs play a critical instructive role in the generation and differentiation of forebrain GABAergic neurons. Like other cell type-specific TFs, DLX1/2 bind to pREs throughout the genome, simultaneously repressing stem and alternative cell fates and promoting genes required for neuronal maturation. To determine whether DLX proteins accomplish this in part through regulation of chromatin state at REs, we screened several members of the NuRD repressive complex and identified an interaction between DLX1 and RBBP4/RBBP7. We performed genome-wide profiling of six members of the NuRD complex to identify a set of high-confidence loci bound by NuRD and DLX1 and found that these loci are primarily pREs near genes involved in the generation of neurons. Using ATAC-seq on sorted cells, we observed that as VZ cells differentiate, many pREs undergo decommissioning by reducing chromatin accessibility. This process of decommissioning is impeded in *Dlx1/2*$^{-/-}$ mutants and reducing levels of *Dlx1/2* together with *Rbbp4* leads to a derepression of *Olig2*. These analyses lead us to conclude that DLX1 binds to the NuRD complex through RBBP4/7 at pREs, altering chromatin state and repressing the transcriptional program for VZ progenitors and oligodendrocytes. Below, we discuss the implications of our findings and speculate on the mechanism by which DLX in conjunction with the NuRD complex controls cell fate.

6A. Interactions of RBBP4/7 with DLX1 and other TFs.

Several TFs including BCL11A, FOG1, PHF6, PRDM16, and SALL1 have RBBP4 binding motifs with a high density of Lysine and Arginine residues (Moody et al., 2018; Basta et al., 2017; Hong et al., 2005; Liu et al., 2015; Ivanochko et al., 2019; Sankaran et al., 2008). Crystal structures show that these positively charged domains bind a negatively charged interface within a central domain of RBBP4 (Moody et al, 2018; Ivanochko et al, 2019). In this study, we identified a similar motif, immediately adjacent to the homeodomain of DLX1, which promotes an interaction with RBBP4/7 (**Figure 2.4**). Alanine substitution of critical Arginine and Lysine residues within this interaction domain severely reduced DLX1's interaction with RBBP4 (**Fig. 2.4E, 2.4F**). A similar

biochemical Alanine scan of the RBBP4 binding motif of SALL4 found that double mutations within the sequence “RRK” abolished binding to RBBP4 (Liu et al. 2018). Comparison of known RBBP4 binding motifs suggest that other than the sequence RK, there is very little sequence specificity required for binding to RBBP4 (**Figure 2.4A**). This preference for charge, rather than sequence, may provide flexibility to the NuRD complex to interact with additional families of TFs, or other proteins, without the need for conservation or convergent evolution of a strict binding sequence.

Interestingly, RBBP4 seems to have different affinities for various posttranslational modifications of Histone H3 (Millard et al. 2016). Additionally, posttranslational modification of an RK moiety of MTA1 mediates its interaction with the NuRD complex (Wang et al., 2009). This poses the question of whether RBBP4 interaction motifs can be posttranslationally modified by enzymes such as LSD1 and G9a, which control arginine methylation of both H3K27 and MTA1 (Bedford and Clark, 2009). Further studies will be needed to discover how RBBP4/7 binding affinity impacts targeting of the NuRD complex to different protein substrates.

6B. *Rbbp4/7* Promote the Progenitor State in the developing MGE and Cortex

To better understand the functions of *Rbbp4/7* in telencephalic development, we studied phenotypes in *Rbbp7 and Rbbp4; Rbbp7* mutants. Our findings support previous evidence that *Rbbp4* constitutive mutants are embryonic lethal (Miao, Biol Repro 2020; Zhao, Epigenetics 2020). Unlike *Rbbp4*$^{-/-}$, loss of the X-linked gene *Rbbp7* is lethal only in female mice (**Figure 3.2**). Hemizygous loss of *Rbbp7* in males has little to no impact on viability, but homozygous loss in females leads to death embryonically observed as late as E16.5. A potential explanation of the sexually dimorphic phenotype of loss of *Rbbp7,* may be its participation in *Xist*-mediated X chromosome inactivation (XCI). The NuRD complex has previously been shown to interact with SPEN, one of the proteins which initiates XCI (Dossin, Nature 2020). This would explain not only the difference in phenotypes between sexes, but also the variability in phenotype severity amongst homozygous null females.

We have not observed a clear MGE phenotype in *Rbbp7* conditional mutants *(Rbbp7 $^{Flox/Y}$, Nkx2-1-Cre)* or *Rbbp4$^{+/-}$* mutants (data not shown). Given that *Rbbp4 and Rbbp7* have high sequence similarity (88% identity in mouse) and overlapping patterns of expression in telencephalic progenitors (Figure 1E), we hypothesized that they have some redundant functions. Indeed, *Rbbp7 $^{Flox/Y,}$ Rbbp4$^{+/-}$* cKOs have robust defects in telencephalic progenitor zones (**Figures 3.3-3.6**). Conditional mutants using MGE or cortical lineage-specific Cre drivers had reduced numbers of PH3^{+} progenitors and a reduction in VZ length (**Figures 3.4, 3.5)**. This depletion leads to a reduction in cortical interneuron numbers at E15 and E16 (**Figure 3.6**). Thus, we propose that RBBP4/7 and the NuRD complex assist in maintaining VZ stem cell pool by promoting cell division in radial glia.

6C. Genomic Co-Occupancy of DLX1 with the NuRD Complex in the Developing Basal Ganglia

Many subunits of the NuRD complex have been associated with transcriptional repression (Cismasiu et al. 2005; Hong et al., 2005; Musselman et al., 2012; Ramírez et al., 2012). The inclusion of HDAC1/2 as central components of NuRD further reinforce this assertion, as Histone deacetylation is often implicated in epigenetic silencing (Hayakawa and Nakayama, 2011; Kennedy et al, 2013). Loss of function studies of other NuRD subunits, however, have suggested that in some instances NuRD may promote gene expression (Ingram et al., 2013; Nitarska et al., 2016; Zhang et al, 2018).

As part of this study, we have performed ChIP-seq for 6 different core subunits of NuRD in the E13.5 ganglionic eminences: CHD4, HDAC1, HDAC2, MBD3, RBBP4 and RBBP7. As expected, we observed a strong correlation in the patterns of genomic occupancy of these NuRD subunits (**Figure 4.1**). We observed some notable differences in genome occupancy between subunits as well, namely that more than 80% of HDAC1/2 peaks were found at promoters (+/- 5kb from TSS), and that RBBP7 bound to a larger proportion of intronic and intergenic peaks than

its paralog RBBP4, despite having fewer called peaks (67% vs. 46%). Interestingly, we observed that all tested NuRD subunits were associated with regions of accessible chromatin (ATAC-seq peaks) and to regions marked by the active mark H3K27ac, rather than the repressive mark H3K27me3 (**Figure 4.1A**). These include pREs and promoters of genes which are highly expressed in the E13.5 BG, including the promoters and known REs of the *Dlx1,2,5,6* genes.

We also find that a high percentage of sites bound by both DLX1 and NuRD are pREs located near TF genes which are regulated by DLX1/2 (**Figure 4.2C**). Previous studies of DLX binding at multiple embryonic stages identified loci where DLX occupancy was associated with transcriptional and epigenetic changes (Lindtner et al., 2019). In this study, loci associated with transcriptional repression were highly enriched for other TFs, while loci associated with active transcription were nearby both TFs and lineage-specific genes (e.g. Gad2, Nrxn3). Because the expression of genes is often regulated by multiple enhancers, which are thought to modulate or restrict the pattern and timing of their expression, binding of DLX1 and NuRD at a regulatory locus may not necessarily always repress transcription. More work will need to be done in examining the impact of combinatorial binding of multiple transcription factors and chromatin modifiers on downstream gene expression. Our findings thus support a model where NuRD cooperates with DLX1 at pREs where the complex may positively or negatively regulate target genes depending on the cellular/genomic context.

6D. Loss of *Dlx1/2* leads to reduced chromatin accessibility at pREs near target genes and derepression of *Olig2*

Previous work has shown that in addition to deregulation of target genes, loss of *Dlx* TFs leads to altered patterns of Histone posttranslational modifications (Lindtner et al., 2019). Because DLX1/2 and NuRD expression overlap in the SVZ, we hypothesized that together they may control epigenetic changes in the transition from stem cell to intermediate progenitor. Here we assessed the impact of the *Dlx1/2*$^{-/-}$ mutation on chromatin accessibility in purified populations

of VZ and SVZ/MZ cells from the E13.5 BG (**Figures 5.1, 5.2**). The majority of changes in chromatin accessibility between WT and *Dlx1/2*$^{-/-}$ mutant samples were in SVZ/MZ cells, where we observed increased accessibility at regions which normally lose accessibility as WT VZ cells mature to SVZ/MZ cells (Figure 6). These regions, termed NDIM peaks, are primarily intergenic and intronic pREs and lie near genes involved in neurogenesis and generation of oligodendrocytes (**Table 5.1**). NDIM peaks that are also bound by DLX1 and NuRD were associated with genes that have increased expression in *Dlx1/2* mutant BG, suggesting that DLX represses gene expression partly through negative regulation of enhancer accessibility.

To test whether this transcriptional repression is mediated through DLX1's interaction with RBBP4, we tested whether reducing the levels of both would impact the expression of a gene that is known to be repressed by *Dlx1/2* and was found to have an NDIM peak bound by DLX1 and NuRD. We identified that VISTA enhancer mm817, which lies near the *Olig1/2* locus, demonstrated activity in the telencephalon and fit these criteria (**Fig 5.3A, 5.3B**). Indeed, we found that reduction in the levels of both *Dlx1/2* and *Rbbp4* together, but not individually, increased the proportion of OLIG2+ cells in the postnatal progenitor zone. This suggests that the restriction of *Olig2* expression to the VZ may be in part regulated by DLX1-mediated silencing of the mm817 pRE through the NuRD complex.

Because the NuRD complex combines two separate functions, it is not clear whether both the histone deacetylation and the nucleosome remodeling functions of the complex can be independently when bound at a specific locus. Studies have shown that a smaller "core" complex consisting of RBBP4/7, MTA1/2/3, and HDAC1/2 binds PWWP2A to the exclusion of CHD, MTA, and GATAD2 proteins, providing one mechanism of controlling the specific action of the complex (Link et al., 2018; Zhang et al. 2018; Low et al., 2020). Due to the variable construction of the complex, slight variations in binding affinity, expression of individual subunits, and overall 3D architecture of chromatin loops are all likely to influence the precise activity of the NuRD complex

at any single locus. Further studies will be needed to understand how TF binding, recruitment of chromatin modifying complexes, and formation of chromatin loops all cooperate to control timing and transcriptional activity on a gene-by-gene basis.

Methods

Transgenic mice

Animal Care and procedures were approved and performed in accordance with National Institutes of Health and the University of California San Francisco Laboratory Animal Research Center (LARC) guidelines. The mouse strain C57BL/6NCrl-Rbbp4em1(IMPC)Mbp/Mmucd, RRID:MMRRC_043433-UCD, was obtained from the Mutant Mouse Resource and Research Center (MMRRC) at University of California at Davis, an NIH-funded strain repository, and was donated to the MMRRC by Kent Lloyd, D.V.M., University of California, Davis. *Rbbp7*$^{tm1a(EUCOMM)Wtsi}$ mice were obtained from the Wellcome Trust Sanger Institute as part of the International Knockout Mouse Consortium program (Skarnes et al., 2011). *Rbbp7*^{Flox} were generated by crossing female *Rbbp7*$^{tm1a(EUCOMM)Wtsi}$ to a male carrying the Beta-actin-FLP allele, and *Rbbp7*^{KO} mice were generated by crossing *Rbbp7*^{Flox} females to a male carrying the Beta-actin-Cre allele. Primers generated to genotype these mice are described below. Genotyping of Dlx1/2$^{-/-}$ mice, Nkx2-1 Cre, Emx1-Cre, and Ai14 alleles was performed as described in Qiu et al. (1995), Xu et al., (2008), Guo et al. (2000) and Madisen et al. (2010) respectively.

ChIP-seq and ATAC-seq experiments were performed on tissue microdissected from *Mus musculus* strain CD1 embryos. The 6 embryos used for ATAC-seq from Dlx1/2$^{-/-}$ embryos were genotyped to balance for sex; 2 males and 1 female was used for each condition. Embryos were not assessed genotypically for gender for ChIP-seq since embryonic tissue from multiple litters was pooled prior to generation of lysates.

Cell culture and immunoprecipitation

HEK293T cells were cultured in DMEM high glucose supplemented with 10% FBS and transfected when cells reached 50-70% confluency using a ratio of 2ul Xtreme-Gene to 1ug plasmid DNA. Cells were harvested 48 hours later using 25mM EDTA in DBPS to dissociate cells prior to addition of lysis buffer (50mM Tris pH 7.5, 150mM NaCl, 1mM EDTA, 0.5% [v/v] Igepal, and 1x Roche complete protease inhibitor). Cell lysates were incubated on ice for 30 minutes then centrifuged for 10 minutes at 10,000 rcf to remove insoluble fraction. For immunoprecipitation, cell lysates were diluted 1:1 with IP buffer (50mM Tris pH 7.5, 150mM NaCl, 1mM EDTA, 0.05% [v/v] Igepal, and 1x Roche complete protease inhibitor) prior to the addition of 40µL Streptactin XT type 3 or M2 anti-FLAG magnetic beads. After incubation with cell lysates overnight at 4°C, beads were washed 5 times with IP buffer and bound proteins were eluted by incubation in Laemmli Sample Buffer at 70°C for 10 minutes.

Cell fractionation and IP from dissected tissue

Microdissected BG from wild type E13.5 embryos were triturated using P1000 tip 10 times to generate single cell suspension. To isolate nuclei, cells were resuspended in 1mL hypotonic lysis buffer (10mM HEPES pH 7.4, 10mM NaCl, 1.5mM $MgCl_2$, 0.5mM DTT, and 1x Roche complete protease inhibitor) per 1E7 cells, held on ice for 10 minutes, and dounced 10-15 times with tight clearance pestle. Nuclei were collected by centrifugation and resuspended in nuclear extraction buffer (20mM HEPES pH 7.4, 300mM NaCl, 25% glycerol, 0.1mM EGTA, 0.02% Igepal, 0.5mM DTT, 250U Benzonase, and 1x Roche complete protease inhibitor) and incubated at 37°C for 15 minutes to digest DNA and RNA. Nuclei were rotated for 30 minutes at 4°C and then centrifuged for 30 minutes at 14,000 x g at 4°C to pellet insoluble fraction. Nuclear extracts were diluted 1:1 with nuclear extraction buffer lacking NaCl for a final concentration of 150mM.

For FLAG tag immunoprecipitations, M2 anti-3XFLAG magnetic beads were washed with IP buffer (see above) and added to nuclear extracts overnight. Beads were washed 5 times with IP buffer and twice with IP buffer lacking Igepal to remove detergent. Proteins were eluted using 100-fold molar excess of 3XFLAG peptide two times and pooled.

For other immunoprecipitations, Dynabeads Protein A (Thermo Fisher, 10001D) were washed twice with IP buffer and added to 5-10µL of antibody suspended in 1% BSA in PBS for two hours at room temperature. Beads were washed twice more with IP buffer and added to nuclear extracts overnight at 4°C. After separation from unbound lysate, beads were washed 5 times with IP buffer and bound proteins were eluted by incubating in 100µL Laemmli Sample Buffer at 70°C for 10 minutes.

Mass Spectroscopy

DLX1 protein was immunoprecipitated as described above except for the elution step from magnetic anti-FLAG beads, which was performed using 30µL of 500µg/mL 3XFLAG peptide and 0.05% RapiGest SF (Waters 186002122) in IP buffer.

Western Blotting

All protein samples were denatured by incubating in Laemmli Sample Buffer at 70°C and separated by SDS-PAGE. Proteins were transferred onto a Hybond-P PVDF membrane (GE Healthcare) using Tris-Glycine Buffer with 20% methanol. Membranes were blocked with 5% milk, and proteins were detected using HRP labeled primary/secondary antibodies or Streptactin-HRP (IBA Biosciences, 2-1502-001) and developed using SuperSignal West Dura Substrate (Thermo Scientific, 34075).

Preparation of brains for sectioning

Embryonic brains for *in situ* hybridization or immunohistochemistry were dissected out in ice cold PBS and drop fixed in 4% paraformaldehyde overnight at 4°C. Postnatal animals were perfused with cold PBS followed by 4% paraformaldehyde and drop fixed in 4% paraformaldehyde overnight at 4°C. Fixed brains were washed twice with cold PBS and then transferred to 30% sucrose in PBS for a minimum of 24 hours. Brains were embedded in O.C.T. compound (Sakura Finetek M71484) and sectioned at 20µm onto glass slides.

***In Situ* Hybridization**

In situ hybridization was performed as in Sandberg et al. 2018. Briefly, slides were washed in PBS, postfixed in 4% PFA, and then acetylated using a solution containing triethanolamine and acetic anhydride. Sections were incubated for one hour in 65°C hybridization buffer (50% Formamide, 5X SSC, 50µg/ml yeast tRNA, 1% SDS, and 50µg/ml Heparin). Digoxigenin-labeled RNA probes were diluted in hybridization buffer and incubated with slides overnight at 65°C. Slides were washed in order with 70°C 5X SSC, twice with 70°C 0.1X SSC, and 3 times with NTT (150mM NaCl, 100mM Tris-HCl, 0.1% Tween-20). Slides were blocked using blocking buffer (1% sheep serum, 2% blocking reagent in NTT) for 1 hour and incubated with 1:10,000 anti-Digoxigenin-AP Fab fragments (Roche 11093274910) overnight at 4°C. Slides were washed three times with NTT and developed using BM purple (Sigma 11442074001) at 37°C.

Immunohistochemistry

Slides were washed twice with PBS and blocked in IHC blocking buffer (1% BSA, 1% sheep serum, 0.2M Glycine in PBS) for one hour at RT. Primary antibodies were resuspended in IHC blocking buffer and incubated 2 hours to overnight. Slides were washed three times for five minutes each with PBST (1X PBS, 0.1% Triton X-100). Alexa Fluor labeled secondary antibodies

were diluted 1:500 in IHC blocking buffer and incubated for one hour before washing 4 times with PBST. Slides were mounted using Aqua-Poly/Mount (Polysciences 18606-5) prior to imaging.

Cell counting

Brain sections were imaged at 10X using an inverted fluorescence microscope and merged using Adobe Photoshop. Cell counting was performed using the cell counting function of Fiji (Schindelin et al. 2012) from 6-7 images per animal.

ChIP-seq

Microdissected E13.5 BG were triturated to generate a single cell suspension. Cells were resuspended in PBS with 5mM DSG and rocked for 15 minutes. The DSG reaction was quenched using 1M Tris pH 7.4 to a final concentration of 100mM. Cells were spun down and resuspended in 1% paraformaldehyde for 10 minutes before quenching reaction with 2.5M Glycine to a final concentration of 250mM. Cell lysis, immunoprecipitation, and library generation was performed as in Lindtner et al. 2019. Libraries were sequenced as single-end 50 nucleotide reads on a Hiseq 4000 (Illumina) at the UCSF Center for Advanced Technology

FlashTag Labeling followed by ATAC-seq

To fluorescently label ventricular cells, E13.5 embryos were removed from uterus in ice cold PBS and CFSE was injected into ventricles and allowed to sit for 20 minutes. For each embryo, ventricles were flushed with PBS and BG were microdissected out and held on ice. Cells were dissociated using papain at 37°C for 10 minutes (Worthington) and cells were sorted into positive and negative populations using FACS. A total of 100,000 cells were collected for positive and negative populations for each embryo, which were then spun down and split into two separate tubes. Lysis, transposition reaction, elution, and amplification were performed as in Buenrostro et al. (2015). Final purification of amplified DNA was carried out using AMPure XP beads (Beckman

Coulter) and sequenced as paired-end 100 nucleotide reads on a Hiseq 4000 (Illumina) at the UCSF Center for Advanced Technology.

ATAC-seq and ChIP-seq Data Analysis

Illumina adapter sequences were removed from reads in FASTQ files using Trim Galore (v0.6.4; Krueger, 2015) and mapped to the mouse genome (GRCm38) using the Burrows-Wheeler Aligner (v0.7.17-r1188; Li and Durbin, 2009). Duplicate reads were removed and resulting data was converted to the BAM format using Samtools (v1.10; Li et al. 2009). Peak calling of enriched regions for ChIP-seq was performed using MACS2 (v2.2.7.1; Zhang et al. 2008) using a broad-cutoff value of 1e-5. Enriched regions were also called for ATAC-seq data using MACS2 using the BAMPE parameter and a p-value cutoff of 1e-5. BigWig file generation, Correlation coefficient heatmaps, ChIP region heatmaps, and k-means clustering were all produced using DeepTools (v3.4.3; Ramirez, 2014). Genomic tracks and called peaks were visualized using the Integrated Genomics Viewer (Robinson et al., 2011). Annotation of ChIP peaks for genomic location was performed using GREAT (McLean et al. 2010) and the R/Bioconductor package Chipseeker (Yu, 2015). Gene Ontology term enrichment was also performed using GREAT.

Genotyping primers used in this study

Rbbp4^{em1}

R4/f: CCTGCCTCATGTGCCTTAGT

R4_WT/rc: AGGACTCTTCCGGGATGGAA

R4_KO/rc: AGTGGTTGTGGGGTTACTTGA

Rbbp7^{tm1a}:

Neo/f CTTGGGTGGAGAGGCTATTC

Neo/rc AGGTGAGATGACAGGAGATC

Rbbp7^{Flox}:

FRTus/f AAGGCGCATAACGATACCAC

R7i3/rc AATGAACTGATGGCGAGCTCA

Rbbp7^{KO}

R7i2/f: TGGTGGTTGCTCGAGTTCAT

R7i3/rc: TCAATGTCCCATGACCCTCTTATT

R7KO/rc: AATGAACTGATGGCGAGCTCAGACC

Antibodies used in this study:

CHD4 (Santa Cruz Biotechnology, sc-11378)

CHD4 (Abcam, ab72418)

DLX1 (in house)

EZH2 (BD, 612666)

HDAC1 (Bethyl, A300-713A)

HDAC2 (Bethyl, A300-705A)

MBD3 (Bethyl, A302-528A)

M2 anti-FLAG (Sigma, F1804)

OLIG2 (Millipore, AB9610)

Phospho-Histone H3 (Millipore, 06-570)

RBBP4 (GeneTex, GTX70232)

RBBP7 (Life Technologies, MA5-25735)

Funding

This work was supported by research grants to JLR from Nina Ireland, NIMH R01MH049428, and to JDP from the NIHCD Predoctoral Training in Developmental Biology, T32HD007470. Funding for the VISTA Enhancer Browser was provided by grant HL066681, Berkeley-PGA, under the Programs for Genomic Applications, funded by National Heart, Lung, & Blood Institute, HG003988 funded by National Human Genome Research Institute, NS062859 funded by National Institute of Neurological Disorders and Stroke, and DE020060 funded by National Institute of Dental and Craniofacial Research.

References

Alvarez-Buylla, A., & Lim, D. A. (2004). For the long run: maintaining germinal niches in the adult brain. *Neuron*, *41*(5), 683-686.

Anderson, S. A., Eisenstat, D. D., Shi, L., & Rubenstein, J. L. R. (1997). Interneuron migration from basal forebrain to neocortex: dependence on Dlx genes. Science, 278(5337), 474-476.

Bannister, A. J., & Kouzarides, T. (2011). Regulation of chromatin by histone modifications. Cell research, 21(3), 381-395.

Basta, J. M., Robbins, L., Denner, D. R., Kolar, G. R., & Rauchman, M. (2017). A Sall1-NuRD interaction regulates multipotent nephron progenitors and is required for loop of Henle formation. Development, 144(17), 3080-3094.

Bedford, M. T., & Clarke, S. G. (2009). Protein arginine methylation in mammals: who, what, and why. *Molecular cell*, *33*(1), 1-13.

Blanco, E., González-Ramírez, M., Alcaine-Colet, A., Aranda, S., & Di Croce, L. (2020). The bivalent genome: characterization, structure, and regulation. Trends in Genetics, 36(2), 118-131.

Bonn, S., Zinzen, R. P., Girardot, C., Gustafson, E. H., Perez-Gonzalez, A., Delhomme, N., ... & Furlong, E. E. (2012). Tissue-specific analysis of chromatin state identifies temporal signatures of enhancer activity during embryonic development. Nature genetics, 44(2), 148-156.

Buenrostro, J. D., Wu, B., Chang, H. Y., & Greenleaf, W. J. (2015). ATAC-seq: a method for assaying chromatin accessibility genome-wide. *Current protocols in molecular biology*, *109*(1), 21-29.

Cao, R., Wang, L., Wang, H., Xia, L., Erdjument-Bromage, H., Tempst, P., ... & Zhang, Y. (2002). Role of histone H3 lysine 27 methylation in Polycomb-group silencing. Science, 298(5595), 1039-1043.

Cismasiu, V. B., Adamo, K., Gecewicz, J., Duque, J., Lin, Q., & Avram, D. (2005). BCL11B functionally associates with the NuRD complex in T lymphocytes to repress targeted promoter. *Oncogene*, *24*(45), 6753-6764.

Creyghton, M. P., Cheng, A. W., Welstead, G. G., Kooistra, T., Carey, B. W., Steine, E. J., ... & Boyer, L. A. (2010). Histone H3K27ac separates active from poised enhancers and predicts developmental state. Proceedings of the National Academy of Sciences, 107(50), 21931-21936.

De Rubeis, S., He, X., Goldberg, A. P., Poultney, C. S., Samocha, K., Cicek, A. E., ... & Singh, T. (2014). Synaptic, transcriptional and chromatin genes disrupted in autism. *Nature*, *515*(7526), 209-215.

Dossin, F., Pinheiro, I., Żylicz, J. J., Roensch, J., Collombet, S., Le Saux, A., ... & Dingli, F. (2020). SPEN integrates transcriptional and epigenetic control of X-inactivation. *Nature*, *578*(7795), 455-460.

Dubois-Chevalier, J., Mazrooei, P., Lupien, M., Staels, B., Lefebvre, P., & Eeckhoute, J. (2018). Organizing combinatorial transcription factor recruitment at cis-regulatory modules. *Transcription*, *9*(4), 233-239.

Eisenstat, D. D., Liu, J. K., Mione, M., Zhong, W., Yu, G., Anderson, S. A., ... & Rubenstein, J. L. (1999). DLX-1, DLX-2, and DLX-5 expression define distinct stages of basal forebrain differentiation. Journal of Comparative Neurology, 414(2), 217-237.

Feledy, J. A., Sargent, T. D., Morasso, M. I., & Jang, S. I. (1999). Transcriptional activation by the homeodomain protein distal-less 3. *Nucleic acids research*, *27*(3), 764-770.

García, M. T., & Harwell, C. C. (2017). Radial glia in the ventral telencephalon. FEBS letters, 591(24), 3942-3959.

Govindan, S., Oberst, P., & Jabaudon, D. (2018). In vivo pulse labeling of isochronic cohorts of cells in the central nervous system using FlashTag. *Nature Protocols*, *13*(10), 2297-2311.

Guo, H., Hong, S., Jin, X. L., Chen, R. S., Avasthi, P. P., Tu, Y. T., ... & Li, Y. (2000). Specificity and efficiency of Cre-mediated recombination in Emx1–Cre knock-in mice. *Biochemical and biophysical research communications*, *273*(2), 661-665.

Hayakawa, T., & Nakayama, J. I. (2011). Physiological roles of class I HDAC complex and histone demethylase. *Journal of Biomedicine and Biotechnology*, *2011*.

Hernández-Miranda, L. R., Parnavelas, J. G., & Chiara, F. (2010). Molecules and mechanisms involved in the generation and migration of cortical interneurons. *ASN neuro*, *2*(2), AN20090053.

Hirabayashi, Y., & Gotoh, Y. (2010). Epigenetic control of neural precursor cell fate during development. Nature Reviews Neuroscience, 11(6), 377-388.

Hong, W., Nakazawa, M., Chen, Y. Y., Kori, R., Vakoc, C. R., Rakowski, C., & Blobel, G. A. (2005). FOG-1 recruits the NuRD repressor complex to mediate transcriptional repression by GATA-1. The EMBO journal, 24(13), 2367-2378.

Hsieh, J., & Gage, F. H. (2005). Chromatin remodeling in neural development and plasticity. Current opinion in cell biology, 17(6), 664-671.

Ivanochko, D., Halabelian, L., Henderson, E., Savitsky, P., Jain, H., Marcon, E., ... & Filippakopoulos, P. (2019). Direct interaction between the PRDM3 and PRDM16 tumor suppressors and the NuRD chromatin remodeling complex. *Nucleic acids research*, *47*(3), 1225-1238.

Iwafuchi-Doi, M., Donahue, G., Kakumanu, A., Watts, J. A., Mahony, S., Pugh, B. F., ... & Zaret, K. S. (2016). The pioneer transcription factor FoxA maintains an accessible nucleosome configuration at enhancers for tissue-specific gene activation. Molecular cell, 62(1), 79-91.

James T. Robinson, Helga Thorvaldsdóttir, Wendy Winckler, Mitchell Guttman, Eric S. Lander, Gad Getz, Jill P. Mesirov. Integrative Genomics Viewer. Nature Biotechnology 29, 24–26 (2011)

Kennedy, P. J., Feng, J., Robison, A. J., Maze, I., Badimon, A., Mouzon, E., ... & Bassel-Duby, R. (2013). Class I HDAC inhibition blocks cocaine-induced plasticity by targeted changes in histone methylation. *Nature neuroscience*, *16*(4), 434-440.

Kim, T. W., Kang, B. H., Jang, H., Kwak, S., Shin, J., Kim, H., ... & Kim, S. Y. (2015). Ctbp2 modulates NuRD-mediated deacetylation of H3K27 and facilitates PRC2-mediated H3K27me3 in active embryonic stem cell genes during exit from pluripotency. Stem Cells, 33(8), 2442-2455.

Kuzmichev, Andrei, et al. "Histone methyltransferase activity associated with a human multiprotein complex containing the Enhancer of Zeste protein." *Genes & development* 16.22 (2002): 2893-2905

Le Guezennec, X., Vermeulen, M., Brinkman, A. B., Hoeijmakers, W. A., Cohen, A., Lasonder, E., & Stunnenberg, H. G. (2006). MBD2/NuRD and MBD3/NuRD, two distinct complexes with different biochemical and functional properties. Molecular and cellular biology, 26(3), 843-851.

Lim, L., Mi, D., Llorca, A., & Marín, O. (2018). Development and functional diversification of cortical interneurons. Neuron, 100(2), 294-313.

Lindtner, S., Catta-Preta, R., Tian, H., Su-Feher, L., Price, J. D., Dickel, D. E., ... & Pennacchio, L. A. (2019). Genomic resolution of DLX-orchestrated transcriptional circuits driving development of forebrain GABAergic neurons. Cell reports, 28(8), 2048-2063.

Link, S., Spitzer, R. M., Sana, M., Torrado, M., Völker-Albert, M. C., Keilhauer, E. C., ... & Nist, A. (2018). PWWP2A binds distinct chromatin moieties and interacts with an MTA1-specific core NuRD complex. Nature communications, 9(1), 1-16.

Liu, B. H., Jobichen, C., Chia, C. B., Chan, T. H. M., Tang, J. P., Chung, T. X., ... & Tan, Y. S. (2018). Targeting cancer addiction for SALL4 by shifting its transcriptome with a pharmacologic peptide. *Proceedings of the National Academy of Sciences*, *115*(30), E7119-E7128.

Liu, Z., Li, F., Zhang, B., Li, S., Wu, J., & Shi, Y. (2015). Structural basis of plant homeodomain finger 6 (PHF6) recognition by the retinoblastoma binding protein 4 (RBBP4) component of the nucleosome remodeling and deacetylase (NuRD) complex. *Journal of Biological Chemistry*, *290*(10), 6630-6638.

Long, H. K., Prescott, S. L., & Wysocka, J. (2016). Ever-changing landscapes: transcriptional enhancers in development and evolution. Cell, 167(5), 1170-1187.

Long, J. E., Cobos, I., Potter, G. B., & Rubenstein, J. L. (2009). Dlx1&2 and Mash1 transcription factors control MGE and CGE patterning and differentiation through parallel and overlapping pathways. Cerebral cortex, 19(suppl_1), i96-i106.

Low, J. K., Silva, A. P., Tabar, M. S., Torrado, M., Webb, S. R., Parker, B. L., ... & Jackman, M. J. (2020). The Nucleosome Remodeling and Deacetylase complex has an asymmetric, dynamic, and modular architecture. C*ell reports, 33*(9), 108450

Madisen, L., Zwingman, T. A., Sunkin, S. M., Oh, S. W., Zariwala, H. A., Gu, H., ... & Lein, E. S. (2010). A robust and high-throughput Cre reporting and characterization system for the whole mouse brain. *Nature neuroscience*, *13*(1), 133.

Marín, O., & Rubenstein, J. L. (2001). A long, remarkable journey: tangential migration in the telencephalon. *Nature Reviews Neuroscience*, *2*(11), 780-790.

Miao, X., Sun, T., Barletta, H., Mager, J., & Cui, W. (2020). Loss of RBBP4 results in defective inner cell mass, severe apoptosis, hyperacetylated histones and preimplantation lethality in mice. *Biology of Reproduction*.

Millard, C. J., Varma, N., Saleh, A., Morris, K., Watson, P. J., Bottrill, A. R., ... & Schwabe, J. W. (2016). The structure of the core NuRD repression complex provides insights into its interaction with chromatin. *Elife*, *5*, e13941.

Moody, R. R., Lo, M. C., Meagher, J. L., Lin, C. C., Stevers, N. O., Tinsley, S. L., ... & Sun, D. (2018). Probing the interaction between the histone methyltransferase/deacetylase subunit RBBP4/7 and the transcription factor BCL11A in epigenetic complexes. Journal of Biological Chemistry, 293(6), 2125-2136.

Moore, L. D., Le, T., & Fan, G. (2013). DNA methylation and its basic function. Neuropsychopharmacology, 38(1), 23-38.

Musselman, C. A., Ramírez, J., Sims, J. K., Mansfield, R. E., Oliver, S. S., Denu, J. M., ... & Kutateladze, T. G. (2012). Bivalent recognition of nucleosomes by the tandem PHD fingers of the CHD4 ATPase is required for CHD4-mediated repression. *Proceedings of the National Academy of Sciences*, *109*(3), 787-792.

Narlikar, G. J., Sundaramoorthy, R., & Owen-Hughes, T. (2013). Mechanisms and functions of ATP-dependent chromatin-remodeling enzymes. Cell, 154(3), 490-503.

Nitarska, J., Smith, J. G., Sherlock, W. T., Hillege, M. M., Nott, A., Barshop, W. D., ... & Riccio, A. (2016). A functional switch of NuRD chromatin remodeling complex subunits regulates mouse cortical development. Cell reports, 17(6), 1683-1698.

Nord, A. S., Pattabiraman, K., Visel, A., & Rubenstein, J. L. (2015). Genomic perspectives of transcriptional regulation in forebrain development. *Neuron*, *85*(1), 27-47.

Panganiban, G., & Rubenstein, J. L. (2002). Developmental functions of the Distal-less/Dlx homeobox genes. *Development*, *129*(19), 4371-4386.

Pavlopoulos, E., Jones, S., Kosmidis, S., Close, M., Kim, C., Kovalerchik, O., ... & Kandel, E. R. (2013). Molecular mechanism for age-related memory loss: the histone-binding protein RbAp48. *Science translational medicine*, *5*(200), 200ra115-200ra115.

Petryniak, M. A., Potter, G. B., Rowitch, D. H., & Rubenstein, J. L. (2007). Dlx1 and Dlx2 control neuronal versus oligodendroglial cell fate acquisition in the developing forebrain. Neuron, 55(3), 417-433.

Pla, R., Stanco, A., Howard, M. A., Rubin, A. N., Vogt, D., Mortimer, N., ... & Nord, A. S. (2018). Dlx1 and Dlx2 promote interneuron GABA synthesis, synaptogenesis, and dendritogenesis. *Cerebral Cortex*, *28*(11), 3797-3815.

Qiu, M., Bulfone, A., Martinez, S., Meneses, J. J., Shimamura, K., Pedersen, R. A., & Rubenstein, J. L. (1995). Null mutation of Dlx-2 results in abnormal morphogenesis of proximal first and second branchial arch derivatives and abnormal differentiation in the forebrain. Genes & development, 9(20), 2523-2538.

Rada-Iglesias, A., Bajpai, R., Swigut, T., Brugmann, S. A., Flynn, R. A., & Wysocka, J. (2011). A unique chromatin signature uncovers early developmental enhancers in humans. Nature, 470(7333), 279-283.

Ramírez, J., Dege, C., Kutateladze, T. G., & Hagman, J. (2012). MBD2 and multiple domains of CHD4 are required for transcriptional repression by Mi-2/NuRD complexes. *Molecular and cellular biology*, *32*(24), 5078-5088.

Sanders, S. J., He, X., Willsey, A. J., Ercan-Sencicek, A. G., Samocha, K. E., Cicek, A. E., ... & Goldberg, A. P. (2015). Insights into autism spectrum disorder genomic architecture and biology from 71 risk loci. *Neuron*, *87*(6), 1215-1233.

Sankaran, V. G., Menne, T. F., Xu, J., Akie, T. E., Lettre, G., Van Handel, B., ... & Orkin, S. H. (2008). Human fetal hemoglobin expression is regulated by the developmental stage-specific repressor BCL11A. *Science*, *322*(5909), 1839-1842.

Satterstrom, F. K., Kosmicki, J. A., Wang, J., Breen, M. S., De Rubeis, S., An, J. Y., ... & Stevens, C. (2020). Large-scale exome sequencing study implicates both developmental and functional changes in the neurobiology of autism. *Cell*, *180*(3), 568-584.

Schindelin, Johannes, et al. "Fiji: an open-source platform for biological-image analysis." Nature methods 9.7 (2012): 676-682

Schmidberger, J. W., Sharifi Tabar, M., Torrado, M., Silva, A. P., Landsberg, M. J., Brillault, L., ... & Mackay, J. P. (2016). The MTA1 subunit of the nucleosome remodeling and deacetylase complex can recruit two copies of RBBP4/7. Protein Science, 25(8), 1472-1482.

Silberberg, S. N., Taher, L., Lindtner, S., Sandberg, M., Nord, A. S., Vogt, D., ... & Ferran, J. L. (2016). Subpallial enhancer transgenic lines: a data and tool resource to study transcriptional regulation of GABAergic cell fate. Neuron, 92(1), 59-74.

Silbereis, J. C., Nobuta, H., Tsai, H. H., Heine, V. M., McKinsey, G. L., Meijer, D. H., ... & Baraban, S. C. (2014). Olig1 function is required to repress dlx1/2 and interneuron production in Mammalian brain. Neuron, 81(3), 574-587.

Skarnes, W. C., Rosen, B., West, A. P., Koutsourakis, M., Bushell, W., Iyer, V., ... & Jackson, D. (2011). A conditional knockout resource for the genome-wide study of mouse gene function. *Nature*, *474*(7351), 337-342.

Smits, A. H., Jansen, P. W., Poser, I., Hyman, A. A., & Vermeulen, M. (2013). Stoichiometry of chromatin-associated protein complexes revealed by label-free quantitative mass spectrometry-based proteomics. Nucleic acids research, 41(1), e28-e28.

Spengler, D., & Hoffmann, A. (2019). Chromatin remodeling complex NuRD in neurodevelopment and neurodevelopmental disorders. *Frontiers in genetics*, *10*, 682.

Spruijt, C. G., Luijsterburg, M. S., Menafra, R., Lindeboom, R. G., Jansen, P. W., Edupuganti, R. R., ... & Mensinga, A. (2016). ZMYND8 co-localizes with NuRD on target genes and regulates poly (ADP-ribose)-dependent recruitment of GATAD2A/NuRD to sites of DNA damage. Cell reports, 17(3), 783-798.

Tang, T., Zhang, Y., Wang, Y., Cai, Z., Lu, Z., Li, L., ... & Seiser, C. (2019). HDAC1 and HDAC2 regulate intermediate progenitor positioning to safeguard neocortical development. *Neuron*, *101*(6), 1117-1133.

Tyler, J. K., & Kadonaga, J. T. (1999). The “dark side” of chromatin remodeling: repressive effects on transcription. Cell, 99(5), 443-446.

Wang, Y., Zhang, H., Chen, Y., Sun, Y., Yang, F., Yu, W., ... & Li, R. (2009). LSD1 is a subunit of the NuRD complex and targets the metastasis programs in breast cancer. *Cell*, *138*(4), 660-672.

Wu, L. M. N., Wang, J., Conidi, A., Zhao, C., Wang, H., Ford, Z., ... & Zwijsen, A. (2016). Zeb2 recruits HDAC–NuRD to inhibit Notch and controls Schwann cell differentiation and remyelination. Nature neuroscience, 19(8), 1060-1072.

Xu, Q., Tam, M., & Anderson, S. A. (2008). Fate mapping Nkx2. 1-lineage cells in the mouse telencephalon. *Journal of Comparative Neurology*, *506*(1), 16-29.

Zerucha, T., Stühmer, T., Hatch, G., Park, B. K., Long, Q., Yu, G., ... & Ekker, M. (2000). A highly conserved enhancer in the Dlx5/Dlx6Intergenic region is the site of cross-regulatory interactions betweenDlx genes in the embryonic forebrain. *Journal of neuroscience*, *20*(2), 709-721.

Zhang, T., Wei, G., Millard, C. J., Fischer, R., Konietzny, R., Kessler, B. M., ... & Brockdorff, N. (2018). A variant NuRD complex containing PWWP2A/B excludes MBD2/3 to regulate transcription at active genes. Nature communications, 9(1), 1-14.

Zhang, Y., Ng, H. H., Erdjument-Bromage, H., Tempst, P., Bird, A., & Reinberg, D. (1999). Analysis of the NuRD subunits reveals a histone deacetylase core complex and a connection with DNA methylation. Genes & development, 13(15), 1924-1935.

Zhang, Yi, et al. "The dermatomyositis-specific autoantigen Mi2 is a component of a complex containing histone deacetylase and nucleosome remodeling activities." *Cell* 95.2 (1998): 279-289.

Zhao, P., Wang, H., Wang, H., Dang, Y., Luo, L., Li, S., ... & Zhang, K. (2020). Essential roles of HDAC1 and 2 in lineage development and genome-wide DNA methylation during mouse preimplantation development. *Epigenetics*, *15*(4), 369-385.

Publishing Agreement

It is the policy of the University to encourage open access and broad distribution of all theses, dissertations, and manuscripts. The Graduate Division will facilitate the distribution of UCSF theses, dissertations, and manuscripts to the UCSF Library for open access and distribution. UCSF will make such theses, dissertations, and manuscripts accessible to the public and will take reasonable steps to preserve these works in perpetuity.

I hereby grant the non-exclusive, perpetual right to The Regents of the University of California to reproduce, publicly display, distribute, preserve, and publish copies of my thesis, dissertation, or manuscript in any form or media, now existing or later derived, including access online for teaching, research, and public service purposes.

DocuSigned by:
James Price
20FAEA7EBCFC414...
Author Signature

12/15/2020
Date